Theory of the strongly nonlinear electrodynamic response of graphene: A hot electron model

S. A. Mikhailov [*]

Institute of Physics, University of Augsburg, D-86135 Augsburg, Germany

An electrodynamic response of graphene to a strong electromagnetic radiation is considered. A hot electron model (HEM) is introduced and a corresponding system of nonlinear equations is formulated. Solutions of this system are found and discussed in detail for intrinsic and doped graphene: the hot electron temperature, nonequilibrium electron and hole densities, absorption coefficient, and other physical quantities are calculated as functions of the incident wave frequency ω and intensity I, of the equilibrium chemical potential μ_0, and temperature T_0, scattering parameters, as well as of the ratio $\tau_\epsilon/\tau_{\rm rec}$ of the intraband energy relaxation time τ_ϵ to the recombination time $\tau_{\rm rec}$. The influence of the radiation intensity on the absorption coefficient A at low ($\hbar\omega \lesssim 2|\mu_0|$, $dA/dI > 0$) and high ($\hbar\omega \gtrsim 2|\mu_0|$, $dA/dI < 0$) frequencies is studied. The results are shown to be in good agreement with recent experimental data.

I. INTRODUCTION

The nonlinear electrodynamic response of graphene attracted great attention in recent years. After the pioneering prediction [1] of the strongly nonlinear electrodynamic properties of graphene, a large number of theoretical [2–35] and experimental [36–56] papers have been published. Theoretically, the higher harmonics generation [1–10], the frequency mixing [11–13], the direct current induced second harmonic generation [14], the saturable absorption and Kerr effects [15,16] have been studied. The nonlinear graphene response in magnetic fields [17–19] and the plasma wave related nonlinear effects [12,20,21,23–26] have been also discussed in detail. A nonperturbative quasiclassical theory based on the relaxation time approximation and a quantum perturbation theory of all third-order nonlinear effects have been developed in Ref. [27] and in Refs. [28–30], respectively. Experimentally, the higher harmonics generation [36–40], the four-wave mixing [41–45], the radiation induced absorption changes[46–50], Kerr effect [51–55], the photoconductivity [56], and other nonlinear phenomena have been observed. All of them demonstrated very large absolute values of the nonlinear optical parameters of graphene. The nonlinear electrodynamic properties of graphene can be used in many applications including broadband detection [57–61], electrically tunable modulation of terahertz [62,63] and optical radiation [64,65], mode-locked lasers [66–70], and other [71–73].

The third-order fourth-rank conductivity tensor of graphene $\sigma_{\alpha\beta\gamma\delta}^{(3)}(\omega_1, \omega_2, \omega_3; \mu_0, T_0)$, analytically calculated in the quantum theory [28–30], describes all possible third-order nonlinear effects for arbitrary polarizations and frequencies of the incident waves. Since $\sigma_{\alpha\beta\gamma\delta}^{(3)}$ was calculated within the perturbation theory, it depends, apart from the input frequencies ω_1, ω_2, ω_3, on the equilibrium chemical potential μ_0 and equilibrium temperature T_0. In many nonlinear response experiments, however, the incident radiation is so strong that the system gets excited far beyond the equilibrium state, and the use of parameters μ_0, T_0 becomes not fully relevant. This problem can be partly circumvented by replacing T_0 in the expression for $\sigma_{\alpha\beta\gamma\delta}^{(3)}$ by an effective temperature T which is considered as a fitting parameter and can be (much) larger than T_0; this way to interpret experimental data was used, e.g., in Refs. [40,45,48,56]. However, in general, not only the temperature but also the chemical potentials of electron (μ_e) and hole (μ_h) gases should be considered to be different from μ_0.

The description of a strongly nonequilibrium electron-hole plasma in terms of the quasiequilibrium electron and hole Fermi gases with their own chemical potentials and temperatures [74–77] is justified if the electron-electron, electron-hole, and hole-hole scattering processes (characterized by a typical scattering time τ_{ee}) are more probable than the electron-phonon and electron-impurities ones. There exist theoretical arguments [76,77] and experimental evidences [78–81] that in typical graphene samples this situation is the case indeed.

Although the hot electron model (HEM) has been already used for interpretation of several nonlinear graphene experiments, a comprehensive theory which would analyze different physical situations and would give the opportunity to calculate μ_e, μ_h, and T as a function of different input parameters of the problem is still absent. In this paper we develop such a theory. In Sec. II we introduce a HEM and formulate a system of nonlinear differential equations which allows to calculate μ_e, μ_h, T and other physical quantities characterizing the electron-hole plasma in graphene in the strongly nonequilibrium state. In Sec. III we analyze solutions of this system of equations in doped and intrinsic graphene, as well as compare results of our theory with some experimental data. In Sec. IV the results are summarized and conclusions are drawn.

* sergey.mikhailov@physik.uni-augsburg.de

II. THEORY

A. The system in equilibrium

We consider a graphene monolayer lying at the plane $z = 0$ on top of a dielectric with the dielectric constant κ and the refractive index $n = \sqrt{\kappa}$. The energy spectrum of electrons ($l = 2$) and holes ($l = 1$) in graphene is

$$E_{l\boldsymbol{k}} = (-1)^l \hbar v_F |\boldsymbol{k}|, \qquad (1)$$

where $v_F \approx 10^8$ cm/s is the Fermi velocity and the energy $E_{l\boldsymbol{k}}$ and the wave vector $\boldsymbol{k}$ are counted from one of the Dirac points. In equilibrium (without irradiation) the electron distribution function has the form (the Boltzmann constant $k_B = 1$ is set to be unity everywhere)

$$f_0(E, \mu_0, T_0) = \frac{1}{1 + \exp\left(\frac{E - \mu_0}{T_0}\right)}, \qquad (2)$$

where μ_0 and T_0 are the equilibrium chemical potential and temperature, the same for electrons and holes.

Below, we will analyze two representative cases, with $\mu_0 = -0.2$ eV (doped graphene) and $\mu_0 = 0$ eV (intrinsic graphene). If $\mu_0 = -0.2$ eV then at room temperature $T_0 = 300$ K the equilibrium densities of electrons and holes,

$$n_e^0 = 4.35 \times 10^7 \text{ cm}^{-2}, \quad n_h^0 = 3.12 \times 10^{12} \text{ cm}^{-2} \text{ (doped)}, \qquad (3)$$

differ by almost five orders of magnitude. In intrinsic graphene at $T_0 = 300$ K the densities are

$$n_e^0 = n_h^0 = 8.14 \times 10^{10} \text{ cm}^{-2} \text{ (intrinsic)}. \qquad (4)$$

The equilibrium chemical potential μ_0 can be experimentally varied by the gate voltage.

B. Hot electrons distribution functions

Now we assume that graphene is irradiated by an external electromagnetic wave with the frequency ω and intensity I. The photon energy $\hbar\omega$ can be both larger and smaller than $2|\mu_0|$, and the intensity of radiation is assumed to be so large that the perturbation theory is inapplicable. The photoexcited electrons absorb the wave energy, due to the intraband and interband absorption processes, and relax their energy to the crystal lattice and to the substrate via different scattering processes. We denote the electron-electron (as well as hole-hole and electron-hole) scattering time as τ_{ee}, the momentum and energy *intra*band relaxation times, due to the electron scattering by lattice imperfections (phonons, impurities, etc.), as τ_p and τ_ϵ, and the *inter*band energy relaxation (actually recombination) time as $\tau_{\rm rec}$ (the time $\tau_{\rm rec}$ will be discussed later in Sec. II G). The momentum relaxation time τ_p is typically much smaller than τ_ϵ, $\tau_p \ll \tau_\epsilon$. Further, we will accept a hypothesis [76–81] that the electron-electron scattering time is smaller than τ_p,

$$\tau_{ee} \ll \tau_p \ll \tau_\epsilon; \qquad (5)$$

according to the literature, τ_{ee} is about a few tens of fs, while τ_p is at least 0.1 ps or larger. Under these conditions, shortly

after the excitation *quasi*equilibrium Fermi distributions

$$f(E, \mu_e, \mu_h, T) = \frac{\Theta(E)}{1 + \exp\left(\frac{E - \mu_e}{T}\right)} + \frac{\Theta(-E)}{1 + \exp\left(\frac{E - \mu_h}{T}\right)}, \quad (6)$$

with the electron (μ_e) and hole (μ_h) chemical potentials and the common temperature $T \neq T_0$, are formed in the conduction and valence bands. The distribution functions of electron ($f_e = f$) and holes ($f_h = 1 - f$) then read as

$$f_e(E, \mu_e, T) = \frac{1}{1 + \exp\left(\frac{E - \mu_e}{T}\right)}, \quad E > 0 \qquad (7)$$

$$f_h(E, \mu_h, T) = \frac{1}{1 + \exp\left(\frac{\mu_h - E}{T}\right)}, \quad E < 0. \qquad (8)$$

It is also possible to consider the version of the theory in which the temperatures of the electron and hole gases T_e and T_h are different. This corresponds to a situation in which electron-electron and hole-hole scattering is more likely than electron-hole scattering. As was shown in Ref. [75] this is typically not the case, therefore, we will restrict ourselves by the model with $T_e = T_h = T$.

We have introduced three unknown quantities μ_e, μ_h, and T, and now need equations which would determine their dependencies on the equilibrium parameters μ_0 and T_0, as well as on the frequency and intensity of the incident radiation.

C. Electron and hole densities

The densities of electrons and holes in the strongly nonequilibrium state (6) are determined by the distribution functions (7) and (8) in the usual way,

$$n_e(\mu_e, T) = \frac{g_s g_v}{S} \sum_{\boldsymbol{k}} f_e(E_{2\boldsymbol{k}}, \mu_e, T) = \frac{2T^2}{\pi(\hbar v_F)^2} F_1\left(\frac{\mu_e}{T}\right), \qquad (9)$$

$$n_h(\mu_h, T) = \frac{2T^2}{\pi(\hbar v_F)^2} F_1\left(-\frac{\mu_h}{T}\right), \qquad (10)$$

where $g_s = g_v = 2$ are the spin and valley degeneracies, S is the sample area, and the function $F_n(z)$ is defined as

$$F_n(z) = \int_0^\infty \frac{x^n dx}{1 + \exp(x - z)}. \qquad (11)$$

The equilibrium electron and hole densities (3) and (4) are determined by Eqs. (9) and (10) in which $\mu_e = \mu_h = \mu_0$ and $T = T_0$.

D. Electron and hole energy densities

The energy density of the electron and hole gases per unit area (per cm^2) is determined by

$$\mathcal{E}_e(\mu_e, T) = \frac{g_s g_v}{S} \sum_{\boldsymbol{k}} E_{2\boldsymbol{k}} f_e(E_{2\boldsymbol{k}}, \mu_e, T)$$

$$= \frac{2T^3}{\pi(\hbar v_F)^2} F_2\left(\frac{\mu_e}{T}\right), \qquad (12)$$

$$\mathcal{E}_h(\mu_h, T) = \frac{2T^3}{\pi(\hbar v_F)^2} F_2\left(-\frac{\mu_h}{T}\right). \qquad (13)$$

The total energy of electrons and holes is

$$\mathcal{E}(\mu_e, \mu_h, T) = \mathcal{E}_e(\mu_e, T) + \mathcal{E}_h(\mu_h, T). \tag{14}$$

E. Conductivity

The linear-response conductivity has three contributions (the derivation can be found, e.g., in Ref. [30]): intraband electron, intraband hole, and interband,

$$\sigma^{(1)}(\omega, \mu_e, \mu_h, T) = \sigma^{(1),e}_{\text{intra}}(\omega, \mu_e, T) + \sigma^{(1),h}_{\text{intra}}(\omega, \mu_h, T) \\ + \sigma^{(1)}_{\text{inter}}(\omega, \mu_e, \mu_h, T), \tag{15}$$

where

$$\frac{\sigma^{(1),e}_{\text{intra}}(\omega, \mu_e, T)}{\frac{e^2 g_s g_v}{16\hbar}} = \frac{i}{\pi\hbar T}\int_0^\infty \frac{E\,dE}{\omega + i\gamma_{\text{intra}}(E)}\frac{1}{\cosh^2\left(\frac{E-\mu_e}{2T}\right)}, \tag{16}$$

$$\frac{\sigma^{(1),h}_{\text{intra}}(\omega, \mu_h, T)}{\frac{e^2 g_s g_v}{16\hbar}} = \frac{i}{\pi\hbar T}\int_0^\infty \frac{E\,dE}{\omega + i\gamma_{\text{intra}}(E)}\frac{1}{\cosh^2\left(\frac{E+\mu_h}{2T}\right)}, \tag{17}$$

and

$$\frac{\sigma^{(1)}_{\text{inter}}(\omega, \mu_e, \mu_h, T)}{\frac{e^2 g_s g_v}{16\hbar}} \\ = \frac{-i}{\pi}\int_0^\infty dE \left(\frac{1}{1+\exp\left(\frac{-E-\mu_h}{T}\right)} - \frac{1}{1+\exp\left(\frac{E-\mu_e}{T}\right)}\right) \\ \times \frac{\hbar(\omega+i\gamma_{\text{inter}})}{E^2 - [\hbar(\omega+i\gamma_{\text{inter}})/2]^2}. \tag{18}$$

We discuss these contributions separately.

1. Intraband conductivity

In order to calculate the intraband conductivity (16) and (17) we need a model for the scattering rate $\gamma_{\text{intra}}(E) \equiv 1/\tau_p(E)$, where $\tau_p(E)$ [see Eq. (5)] is the energy-dependent momentum relaxation time due to the scattering of electrons and holes with impurities, phonons, and other lattice imperfections (but not with each other). As a first choice we use for $\gamma_{\text{intra}}(E)$ the model

$$\hbar\gamma_{\text{intra}}(E) = \frac{|E|}{\frac{\zeta}{2} + \sqrt{1 + \frac{E^4}{E_i^4} - 1}} \tag{19}$$

which is discussed in detail in Appendix A. The quantities ζ and E_i in (19) are fitting parameters: ζ is the minimal static conductivity of graphene in the Dirac point, in units e^2/h; $E_i \propto \sqrt{N_i}$ is a Coulomb energy associated with the density of impurities N_i [see (A2)]. The parameters ζ and E_i can be found by fitting the formula (A6) to the experimental data for the gate-voltage dependence of the *static* linear conductivity of graphene (see example in Fig. 13). Thus found parameters ζ and E_i and the model expression (19) are then used in formulas (16) and (17) for the *high-frequency* nonlinear conductivities of graphene. In the rest of the paper we use $\zeta = 4$ and $E_i = 30$ meV, which corresponds to the mobility of about 7260 cm^2/Vs. For the relation between the energy E_i

and the sample mobility, as well as for further discussion of the model (19), see Appendix A.

Alternatively, we also use the energy-independent momentum relaxation rate model with $\gamma_{\text{intra}} = \gamma_p = 1/\tau_p$. Then, the intraband dynamic conductivity assumes the form

$$\frac{\sigma^{(1)}_{\text{intra}}(\omega, \mu_e, \mu_h, T)}{\frac{e^2 g_s g_v}{16\hbar}} \\ = \frac{4i}{\pi}\frac{T}{\hbar(\omega+i\gamma_p)}\left[F_0\left(\frac{\mu_e}{T}\right) + F_0\left(-\frac{\mu_h}{T}\right)\right] \\ = \frac{4i}{\pi}\frac{T}{\hbar(\omega+i\gamma_p)}\ln[(1+e^{\mu_e/T})(1+e^{-\mu_h/T})]. \tag{20}$$

The model (19) better reproduces typical experimental data on the static conductivity of graphene, therefore, we use it in the main part of the paper. The model (20) was used in some experiments (e.g., Ref. [48]) by interpreting the measured data; comparing our results with Ref. [48] in Sec. III we also use the model (20) with the energy-independent momentum relaxation rate γ_{intra}.

2. Interband dynamic conductivity

The interband conductivity (18) depends on the interband scattering rate γ_{inter}. We assume that $\gamma_{\text{inter}} \to 0$ since a finite γ_{inter} does not influence the final result under the condition $\hbar\gamma_{\text{inter}} \ll T$ which is typically satisfied in experiments. Then, Eq. (18) can be simplified so that the real part assumes the form

$$\text{Re}\,\frac{\sigma^{(1)}_{\text{inter}}(\omega, \mu_e, \mu_h, T)}{\frac{e^2 g_s g_v}{16\hbar}} = \frac{\sinh\left(\frac{\hbar|\omega|-(\mu_e-\mu_h)}{2T}\right)}{\cosh\left(\frac{\mu_h+\mu_e}{2T}\right)+\cosh\left(\frac{\hbar|\omega|-(\mu_e-\mu_h)}{2T}\right)} \tag{21}$$

and the imaginary part is expressed in terms of a principal value integral (denoted by $\mathcal{P}$)

$$\text{Im}\,\frac{\sigma^{(1)}_{\text{inter}}(\omega, \mu_e, \mu_h, T)}{\frac{e^2 g_s g_v}{16\hbar}} \\ = -\frac{\hbar\omega}{\pi}\mathcal{P}\int_0^\infty \frac{\sinh\left(\frac{E-(\mu_e-\mu_h)/2}{T}\right)}{\cosh\left(\frac{\mu_h+\mu_e}{2T}\right)+\cosh\left(\frac{E-(\mu_e-\mu_h)/2}{T}\right)} \\ \times \frac{dE}{E^2 - (\hbar\omega/2)^2}. \tag{22}$$

Notice that the real part of the interband conductivity can be negative if $\mu_e > \mu_h$ and $\hbar\omega < (\mu_e - \mu_h)$. Physically, this is due to the population inversion in the nonequilibrium state.

F. Absorption coefficient

We assume that graphene lies on the surface of a dielectric substrate with the dielectric constant κ and the refractive index $n = \sqrt{\kappa}$, and the external radiation with the intensity I is normally incident on the structure. The incident radiation is transmitted through (with the intensity TI), reflected from (the intensity RI), and absorbed in the graphene layer (the intensity AI). The absorbed part of the radiation energy is determined by the absorption coefficient A, sometimes also referred to as absorbance. The coefficient A is determined by

the Joule heating $\boldsymbol{j} \cdot \boldsymbol{E}$ and in the linear-response regime is proportional to the real part of the first-order conductivity $\sigma^{(1)}$. In the nonlinear regime we will assume that the nonlinearity mainly manifests itself in changing the chemical potentials ($\mu_0 \to \mu_e, \mu_h$) and electron temperature ($T_0 \to T$) in formulas (15)–(18) and, hence, in accordance with these equations, the absorption coefficient can be presented in the form

$$A(\omega, \mu_e, \mu_h, T) = A^{\text{intra}}(\omega, \mu_e, \mu_h, T) \\ + A^{\text{inter}}(\omega, \mu_e, \mu_h, T), \quad (23)$$

with intraband

$$A^{\text{intra}}(\omega, \mu_e, \mu_h, T) = A_e^{\text{intra}}(\omega, \mu_e, T) + A_h^{\text{intra}}(\omega, \mu_h, T) \\ = \frac{\frac{4\pi}{c} \operatorname{Re} \sigma_{\text{intra}}^{(1)}(\omega, \mu_e, \mu_h, T)}{\left| \frac{n+1}{2} + \frac{2\pi}{c} \sigma^{(1)}(\omega, \mu_e, \mu_h, T) \right|^2}, \quad (24)$$

and interband

$$A^{\text{inter}}(\omega, \mu_e, \mu_h, T) = \frac{\frac{4\pi}{c} \operatorname{Re} \sigma_{\text{inter}}^{(1)}(\omega, \mu_e, \mu_h, T)}{\left| \frac{n+1}{2} + \frac{2\pi}{c} \sigma^{(1)}(\omega, \mu_e, \mu_h, T) \right|^2} \quad (25)$$

contributions. The denominators in Eqs. (24) and (25) contain the total conductivity. If the substrate is made out of silicon dioxide, then its dielectric constant is $\kappa_{\text{SiO}_2} = 3.9$ and $n = \sqrt{\kappa_{\text{SiO}_2}} = 1.975$.

The absorption coefficient formulas (23)–(25) are approximate. In general, the current $\boldsymbol{j}$ contains the higher contributions $j_\alpha^{(3)} = \sigma_{\alpha\beta\gamma\delta}^{(3)} E_\beta E_\gamma E_\delta$, $j_\alpha^{(5)} = \sigma_{\alpha\beta\gamma\delta\mu\nu}^{(5)} E_\beta E_\gamma E_\delta E_\mu E_\nu$, etc., where all higher-order conductivities should be considered as functions of nonequilibrium chemical potentials μ_e, μ_h and temperature T. However, at present the functions $\sigma^{(5)}$, $\sigma^{(7)}$, etc., are unknown and the function $\sigma_{\alpha\beta\gamma\delta}^{(3)}(\omega_1, \omega_2, \omega_3; \mu_0, T_0)$ was calculated [28–30] only for the quasiequilibrium case with μ_0 and T_0. Therefore, in this paper we restrict ourselves by the approach (23)–(25), postponing developing of more general theories for future publications.

G. Dynamics equations of the hot electron model

Now, we are prepared to formulate the basic equations of our HEM. We will assume that the intraband energy relaxation time τ_ϵ is shorter than the interband recombination time τ_{rec}, $\tau_\epsilon \ll \tau_{\text{rec}}$. This condition is typically satisfied in conventional semiconductors. In graphene the radiative recombination time, according to estimates in Refs. [82,83], is around hundreds of nanoseconds at room temperature, while τ_ϵ lies in the tens-of-ps range. This justifies the use of the condition $\tau_\epsilon \ll \tau_{\text{rec}}$ below.

1. Energy relaxation

Assume that the system is excited by a powerful incident radiation with the intensity I. Since the recombination is a slow process, the electron and hole Fermi gases are independent from each other in the sense that they are characterized (at the time $t \gtrsim \tau_{ee}$ after the excitation is switched on) by their own chemical potentials μ_e and μ_h, and the temperature T. At the longer timescale $t \sim \tau_\epsilon$ the charge carriers, having been scattered by phonons, impurities, and other lattice imperfections, relax their energy to the lattice. We assume that the energy relaxation equations for electrons and holes can then

be written, as it is usually done in semiconductor physics, in the form

$$\frac{\partial \mathcal{E}_e(\mu_e, T)}{\partial t} = A_e^{\text{intra}}(\omega, \mu_e, T) I - \frac{\mathcal{E}_e(\mu_e, T) - \mathcal{E}_e(\mu_e^0, T_0)}{\tau_\epsilon}, \quad (26)$$

$$\frac{\partial \mathcal{E}_h(\mu_h, T)}{\partial t} = A_h^{\text{intra}}(\omega, \mu_h, T) I - \frac{\mathcal{E}_h(\mu_h, T) - \mathcal{E}_h(\mu_h^0, T_0)}{\tau_\epsilon}, \quad (27)$$

meaning that the energy of hot electron and hole gases grows in time due to the intraband absorption in each (conduction and valence) band and relaxes to their steady-state quasiequilibrium energies $\mathcal{E}_e(\mu_e^0, T_0)$ and $\mathcal{E}_h(\mu_h^0, T_0)$ with the characteristic timescale τ_ϵ. We emphasize that the temperature of the relaxed quasiequilibrium state in Eqs. (26) and (27) coincides with the lattice temperature T_0 since τ_ϵ describes the relaxation processes between the charge carrier gases and the lattice. However, the chemical potentials μ_e^0 and μ_h^0 differ from the equilibrium chemical potential μ_0 since the density of electrons and holes are still larger than those in equilibrium since $\tau_\epsilon \ll \tau_{\text{rec}}$. The relation between $\mu_{e,h}$ and T, from one side, and $\mu_{e,h}^0$ and T_0, from the other side, is determined by the conservation of the electron and hole densities

$$n_e(\mu_e, T) = n_e(\mu_e^0, T_0), \quad n_h(\mu_h, T) = n_h(\mu_h^0, T_0). \quad (28)$$

The energy relaxation times τ_ϵ in Eqs. (26) and (27) can, in principle, be different. We will assume, for simplicity, that they are the same. Then, we can take a sum of Eqs. (26) and (27) and get the total energy relaxation equation

$$\frac{\partial \mathcal{E}(\mu_e, \mu_h, T)}{\partial t} = A^{\text{intra}}(\omega, \mu_e, \mu_h, T) I \\ - \frac{\mathcal{E}(\mu_e, \mu_h, T) - \mathcal{E}(\mu_e^0, \mu_h^0, T_0)}{\tau_\epsilon}. \quad (29)$$

2. Recombination

At a longer timescale $\sim \tau_{\text{rec}}$ electrons and holes recombine. Taking into account that they are generated and recombine by pairs,

$$n_e(t) = n_e^0 + \delta n(t), \quad n_h(t) = n_h^0 + \delta n(t), \quad (30)$$

we write the generation-recombination rate equation in the form

$$\frac{\partial n_e}{\partial t} = \frac{\partial n_h}{\partial t} = G - R = \frac{A^{\text{inter}}(\omega, \mu_e, \mu_h, T)}{\hbar\omega} I \\ - \alpha_{\text{rec}}(n_e n_h - n_e^0 n_h^0). \quad (31)$$

The first (generation) term G in the right-hand side of (31) represents the number of electron-hole pairs generated per second on a unit area. It equals the radiation intensity I (the radiation energy *incident* on a unit area per second) times the *interband* absorption coefficient (which gives the energy *absorbed* on a unit area per second due to the electron-hole generation processes), and divided by the photon energy (which results in the number of electron-hole pairs generated on a unit area per second). The second term R in the right-hand side of (31) is the recombination rate. The recombination is a

nonlinear biparticle process with the recombination rate being proportional to the product of electron and hole densities $n_e n_h$. The recombination term describes the relaxation to the equilibrium electron and hole densities $n_e^0 n_h^0$. The recombination coefficient $\alpha_{\rm rec}$ is measured in units cm^2/s and is independent of the particle densities. It is the second (in addition to τ_ϵ) parameter of the theory.

Apart from the recombination coefficient $\alpha_{\rm rec}$ one can also introduce a quantity $\tau_{\rm rec}$ which is measured in units of time and *at low excitation levels* has the meaning of the recombination time (in general, the recombination process is not purely exponential and the meaning of $\tau_{\rm rec}$ is more complicated, see below). Assume that the radiation intensity $I(t)$ is switched off at the time moment $t = 0$ and consider the time evolution of the electron and hole densities $\delta n(t)$ at $t > 0$. Substituting (30) into Eq. (31) with $I = 0$ and taking into account the initial condition $\delta n(0) = \delta n_0$ we get

$$\Delta(t) \equiv \frac{\delta n(t)}{n_e^0 + n_h^0} = \frac{\Delta_0}{(1 + \Delta_0)e^{\alpha_{\rm rec}(n_e^0 + n_h^0)t} - \Delta_0}$$
$$= \frac{\Delta_0}{(1 + \Delta_0)e^{t/\tau_{\rm rec}} - \Delta_0}, \qquad (32)$$

where $\Delta(t)$ is the relative change of the charge carrier density as compared to their total equilibrium density, and $\Delta_0 = \Delta(0)$. The quantity

$$\tau_{\rm rec} = \frac{1}{\alpha_{\rm rec}(n_e^0 + n_h^0)} \qquad (33)$$

has the dimension of time, depends on the total equilibrium density of electrons and holes and determines the time evolution of the electron-hole recombination (32). We emphasize that $\tau_{\rm rec}$ has the meaning of time over which the initial carrier density reduces by a factor of $\sim 2.72 \ldots$ *only at very low excitation levels* $\Delta_0 \ll 1$,

$$\Delta(t) \approx \Delta_0 e^{-t/\tau_{\rm rec}}, \quad \Delta_0 \ll 1 \qquad (34)$$

(see Fig. 1). At high excitation levels $\Delta_0 \gg 1$ or $\delta n_0 \gg (n_e^0 + n_h^0)$, the density $\delta n(t)$ first very quickly decreases, with the time constant $\sim \tau_{\rm rec}/\Delta_0$, down to the values $\sim (n_e^0 + n_h^0)$, and then decays further exponentially (see inset to Fig. 1). Quantitatively, $\Delta(t)$ decreases from its initial value Δ_0 by a factor of 2 during the time $\tau_{\rm rec}/(\Delta_0 + 1) \ll \tau_{\rm rec}$ and by a factor of Δ_0 during the time $\sim \tau_{\rm rec}$.

The generation-recombination rate equation (31) can be also rewritten in the form explicitly containing $\tau_{\rm rec}$:

$$\frac{\partial(\delta n)}{\partial t} = \frac{A^{\rm inter}(\omega, \mu_e, \mu_h, T)}{\hbar\omega} I - \frac{\delta n}{\tau_{\rm rec}}\left(1 + \frac{\delta n}{n_e^0 + n_h^0}\right). \quad (35)$$

3. Preliminary summary and discussion

The recombination of charge carriers in graphene characterized by a more complicated than $e^{-t/\tau}$ decay was commonly observed in time-resolved pump-probe experiments (see, e.g., Refs. [48,84,85] and others). It was often interpreted by introducing two different timescales τ_1 and τ_2 where different τ's were attributed to physically different relaxation mechanisms. As seen from Sec. II G 2 the seemingly double-τ time decay is actually described by a single formula (32) with only one decay-time parameter $\tau_{\rm rec}$. The reason of the more
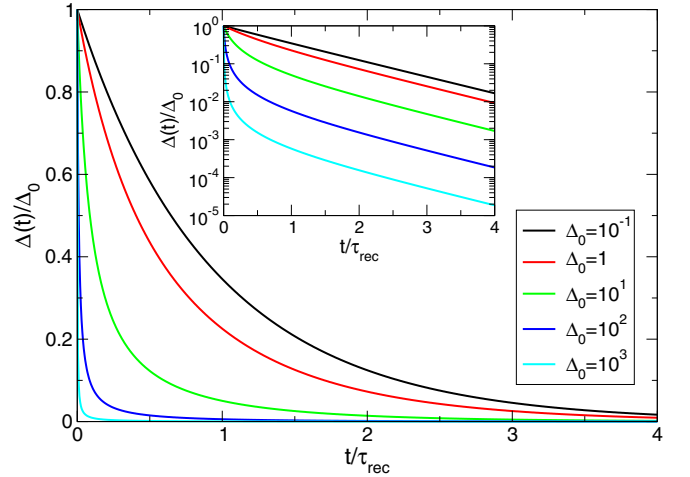

FIG. 1. The time dependence of the normalized electron-hole pairs density $\Delta(t)$, Eq. (32), at different values of Δ_0. The main plot and the inset show the same curves with linear and logarithmic scales of the y axis, respectively. The decay of the electron-hole pairs density is exponential only at low excitation levels $\Delta_0 \ll 1$.

complicated behavior of $\delta n(t)$ is the intrinsically nonlinear nature of the electron-hole recombination process seen in Eqs. (31) and (35). The corresponding two time constants are $\tau_1 = \tau_{\rm rec}/(\Delta_0 + 1)$ and $\tau_2 = \tau_{\rm rec}$. In the strong excitation limit $\Delta_0 \gg 1$ the first time is much shorter than the second one, $\tau_1 \ll \tau_2$; while in the weak excitation limit ($\Delta_0 \ll 1$), the two times merge into one, $\tau_1 \simeq \tau_2 = \tau_{\rm rec}$ (Fig. 1).

The nonlinearity of the recombination process is known in the semiconductor physics, e.g., Ref. [86]. We have briefly reproduced here the nonlinear recombination equations (31) and (35) and the corresponding derivation of Eq. (32) since in some recent papers (e.g., Ref. [40]) a strongly nonequilibrium ($\Delta_0 \gg 1$) recombination dynamics has been improperly described by a linear recombination term $R \propto -\delta n/\tau_{\rm rec}$.

Equations (29) and (35) [or (29) and (31)] describe the dynamics of the electron temperature T, chemical potentials μ_e, μ_h, and all other physical quantities within our HEM. The energy densities $\mathcal{E}_e$, $\mathcal{E}_h$ in Eq. (29), as well as the intraband and interband absorption coefficients $A^{\rm intra}$, $A^{\rm inter}$ in Eqs. (29) and (35), depend on six unknown quantities T, μ_e, μ_h, μ_e^0, μ_h^0, and δn. The four missing equations can be found by inverting the relations (9) and (10), namely,

$$\mu_e = T G\left(\frac{\pi(\hbar v_F)^2 n_e}{2T^2}\right) = T G\left(\frac{\pi(\hbar v_F)^2(n_e^0 + \delta n)}{2T^2}\right), \quad (36)$$

$$\mu_h = -T G\left(\frac{\pi(\hbar v_F)^2 n_h}{2T^2}\right) = -T G\left(\frac{\pi(\hbar v_F)^2(n_h^0 + \delta n)}{2T^2}\right), \quad (37)$$

$$\mu_e^0 = T_0 G\left(\frac{\pi(\hbar v_F)^2(n_e^0 + \delta n)}{2T_0^2}\right), \quad (38)$$

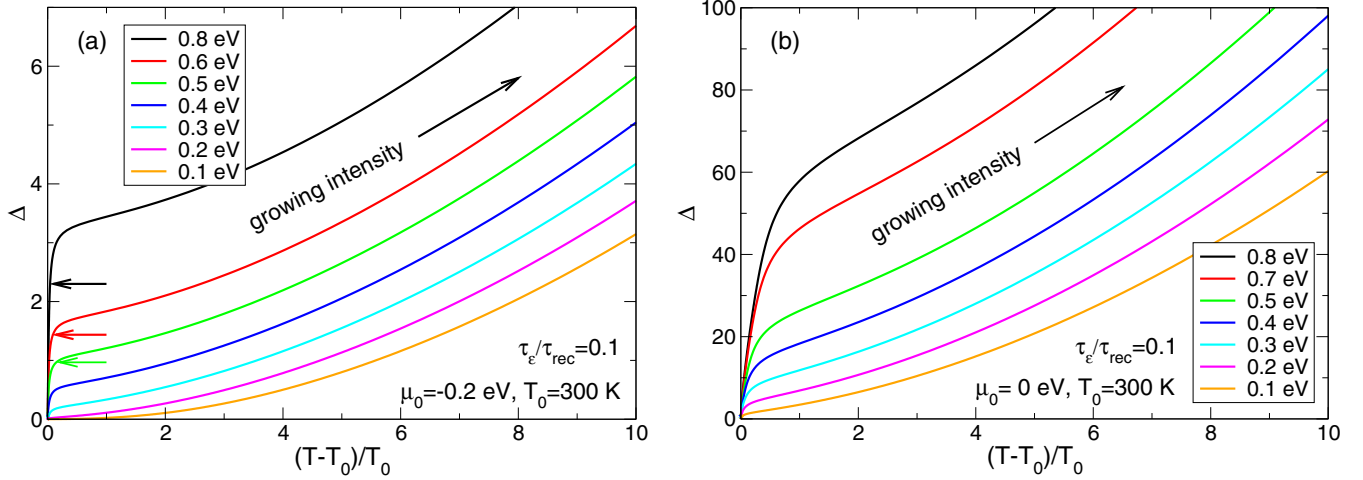$$\mu_h^0 = -T_0 G\left(\frac{\pi(\hbar v_F)^2(n_h^0 + \delta n)}{2T_0^2}\right), \quad (39)$$

FIG. 2. The relative change of the density $\Delta = \delta n/(n_e^0 + n_h^0)$ versus relative change of the temperature $(T - T_0)/T_0$ at different values of the input wave frequency $\hbar\omega$ (in eV). The ratio of the relaxation times is $\tau_\epsilon/\tau_{\mathrm{rec}} = 0.1$, temperature $T_0 = 300$ K, and the energy $E_i = 30$ meV. The equilibrium chemical potential is (a) $\mu_0 = -0.2$ eV and (b) $\mu_0 = 0$ eV. Arrows in (a) show the points where $I/I_0 = 10^5$.

where $G(y)$ is the inverse function of $F_1(x)$,

$$y = F_1(x) \iff x = G(y) \equiv F_1^{-1}(y), \qquad (40)$$

with F_1 defined in (11). Equations (36)–(39), together with (29) and (35), give six equations for six unknown variables. The quantities ω, I, T_0, and μ_0 (or E_F), as well as parameters τ_ϵ and τ_{rec}, are assumed to be known input parameters.

H. Steady-state equations

In the rest of the paper we will analyze the steady-state solutions of Eqs. (29) and (35). Setting $\partial/\partial t = 0$ we get

$$
\begin{aligned}
I &= \frac{\mathcal{E}(\mu_e, \mu_h, T) - \mathcal{E}(\mu_e^0, \mu_h^0, T_0)}{\tau_\epsilon A^{\mathrm{intra}}(\omega, \mu_e, \mu_h, T)} \\
&= \frac{\hbar\omega\delta n}{\tau_{\mathrm{rec}} A^{\mathrm{inter}}(\omega, \mu_e, \mu_h, T)}\left(1 + \frac{\delta n}{n_e^0 + n_h^0}\right). \quad (41)
\end{aligned}
$$

The second equation here does not contain the intensity I. It can be presented in the dimensionless form

$$\mathcal{L}(\hbar\omega, \mu_e, \mu_h, T) = \frac{\tau_\epsilon}{\tau_{\mathrm{rec}}}\mathcal{R}(\hbar\omega, \mu_e, \mu_h, T, \Delta), \qquad (42)$$

where the left- and right-hand sides read as

$$\mathcal{L}(\hbar\omega, \mu_e, \mu_h, T) = \frac{\mathrm{Re}\,\sigma_{\mathrm{inter}}^{(1)}(\omega, \mu_e, \mu_h, T)}{\mathrm{Re}\,\sigma_{\mathrm{intra}}^{(1)}(\omega, \mu_e, \mu_h, E_i, T)}, \qquad (43)$$

$$
\begin{aligned}
&\mathcal{R}(\hbar\omega, \mu_e, \mu_h, T, \Delta) \\
&= \frac{\Delta(1+\Delta)\hbar\omega T_0^2\left[F_1\left(-\frac{\mu_0}{T_0}\right) + F_1\left(\frac{\mu_0}{T_0}\right)\right]}{T^3\left[F_2\left(\frac{\mu_e}{T}\right) + F_2\left(-\frac{\mu_h}{T}\right)\right] - T_0^3\left[F_2\left(\frac{\mu_e^0}{T_0}\right) + F_2\left(-\frac{\mu_h^0}{T_0}\right)\right]}.
\end{aligned}
$$
$$(44)$$

Solving the nonlinear equation (42), together with (36)–(39), we can find the relation between the relative change of the density $\Delta = \delta n/(n_e^0 + n_h^0)$ and the relative change of the temperature $\delta T/T_0 = (T - T_0)/T_0$. Notice that Eq. (42) depends only on the ratio of the characteristic times $\tau_\epsilon/\tau_{\mathrm{rec}}$ and not

on each of them separately. After the relation between Δ and $\delta T/T_0$ is found we substitute it into any of the equations (41) and relate these quantities to the intensity of radiation. This gives two equivalent formulas

$$
\begin{aligned}
\mathcal{P}_a \equiv \frac{I}{I_0} &= \frac{\hbar\omega}{T_0}\frac{\tau_\epsilon}{\tau_{\mathrm{rec}}}\frac{\Delta(1+\Delta)}{A^{\mathrm{inter}}(\omega, \mu_e, \mu_h, T)} \\
&\quad \times \left[F_1\left(\frac{\mu_0}{T_0}\right) + F_1\left(-\frac{\mu_0}{T_0}\right)\right] \quad (45)
\end{aligned}
$$

or

$$
\begin{aligned}
\mathcal{P}_b &= \frac{I}{I_0} \\
&= \frac{(T/T_0)^3\left[F_2\left(\frac{\mu_e}{T}\right) + F_2\left(-\frac{\mu_h}{T}\right)\right] - \left[F_2\left(\frac{\mu_e^0}{T_0}\right) + F_2\left(-\frac{\mu_h^0}{T_0}\right)\right]}{A^{\mathrm{intra}}(\omega, \mu_e, \mu_h, T)},
\end{aligned}
$$
$$(46)$$

where we have introduced a power density unit

$$I_0 = \frac{2T_0^3}{\pi(\hbar v_F)^2\tau_\epsilon} \approx 410\frac{(T_0[\mathrm{K}]/300)^3}{\tau_\epsilon[\mathrm{ps}]}\frac{\mathrm{W}}{\mathrm{cm}^2}, \qquad (47)$$

which does not depend on the charge carrier density. At room temperature the power density unit I_0 is about 400 W/cm^2 if $\tau_\epsilon \simeq 1$ ps. This is a rather small value, i.e., the strongly nonlinear regime corresponds to $I \gg I_0$. Notice that Eqs. (42)–(46) are presented in the explicitly dimensionless form, which means, in particular, that scaling all energies by the same numerical factor will not change the final results. This makes them universal in a sense.

Now, we can start analyzing results which our model gives. We will assume that $T_0 = 300$ K and $\mu_0 = -0.2$ eV and 0 eV for doped and intrinsic graphene, respectively. All energy quantities will be given in eV.
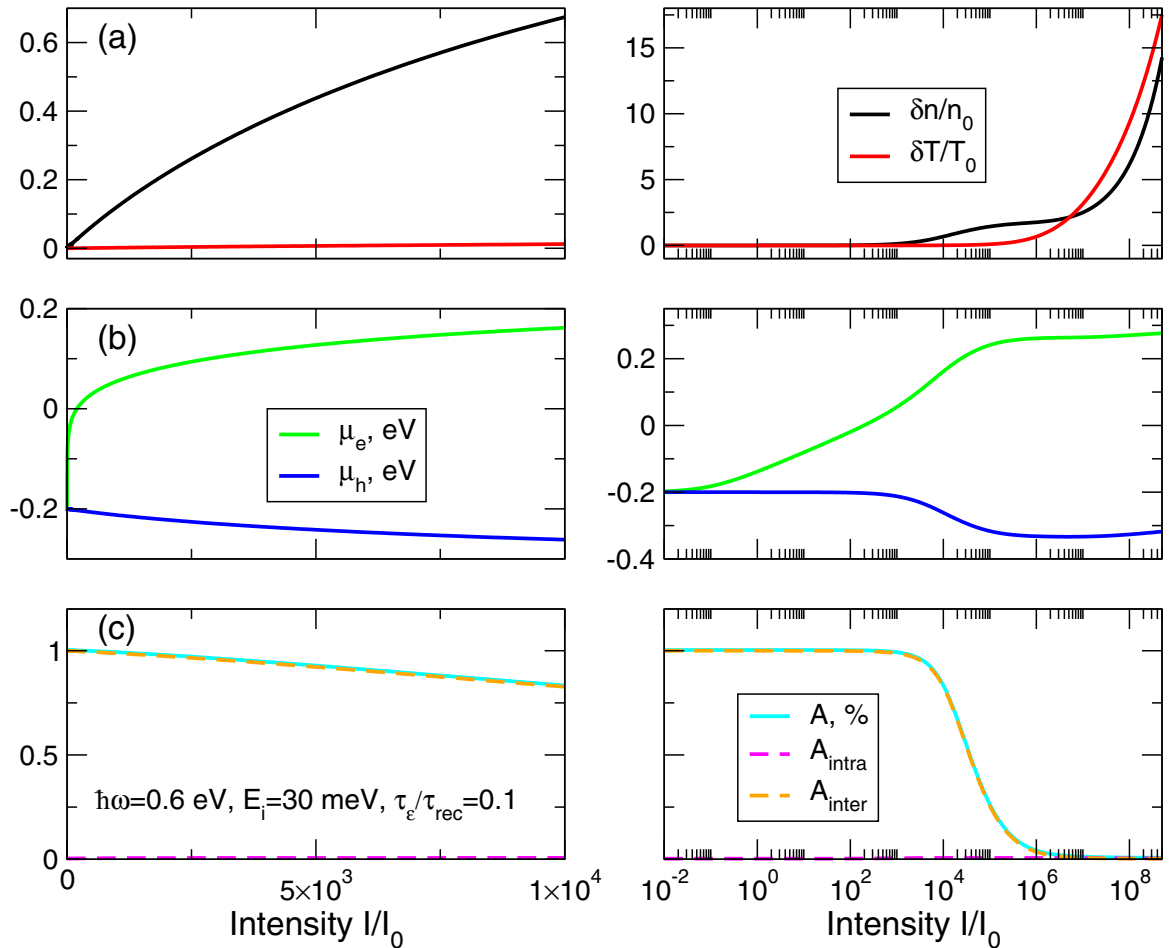
FIG. 3. (a) The relative change of the density $\Delta = \delta n/n_0 = \delta n/(n_e^0 + n_h^0)$ and temperature $(T - T_0)/T_0$, (b) the chemical potentials of electrons and holes μ_e and μ_h, and (c) the absorption coefficient A, together with the intraband and interband contributions, as functions of the dimensionless power density I/I_0 at $\hbar\omega = 0.6$ eV, $E_i = 30$ meV, and $\tau_\epsilon/\tau_{\rm rec} = 0.1$. The equilibrium chemical potential and temperature are $\mu_0 = -0.2$ eV and $T_0 = 300$ K. Left columns show the power dependencies at $I/I_0 < 10^4$, and the right columns the same dependencies in a broader power range. The horizontal axis scale is the same in all left and all right panels. The vertical axis scale is the same in both (c) panels.

III. RESULTS

A. Density-temperature diagrams

Figure 2 shows the density-temperature diagrams obtained by solving Eq. (42) at different frequencies, $T_0 = 300$ K, $\tau_\epsilon/\tau_{\rm rec} = 0.1$, and two different values of the equilibrium chemical potential $\mu_0 = -0.2$ and 0 eV. Each point on each curve corresponds to a certain value of the input wave power density. The low-intensity regime $I/I_0 \ll 1$ corresponds to the origin of the plots where $\Delta \ll 1$ and $\delta T/T_0 \ll 1$. The higher the power, the larger are the relative changes of both the density and the temperature, so that both Δ and $\delta T/T_0$ grow with the increasing intensity. The rate of their growth depends, however, on the frequency.

First, we consider the case $\mu_0 = -0.2$ eV [Fig. 2(a)]. If $\hbar\omega \gtrsim 2|\mu_0| = 0.4$ eV (black to blue curves), i.e., when the *interband* transitions dominate, the relative change of the density Δ, at low intensities, is much stronger than the relative change of the temperature $\delta T/T_0$. When I/I_0 grows from zero up to the values $\sim 10^5$ [see arrows in Fig. 2(a)], Δ increases up to $\Delta \simeq 1$–3, while the temperature remains practically unchanged, $\delta T/T_0 \ll 1$. The values $\Delta \simeq 1$–3

correspond to practically equal densities of photoexcited electrons and holes; remind that at $\mu_0 = -0.2$ eV and $T_0 = 300$ K the equilibrium electron and hole densities differed by almost five orders of magnitude [Eq. (3)]. At even larger intensities, $I/I_0 \gtrsim 10^5$, the hot carrier temperature starts to grow too: in this situation the densities of electrons and holes are large and close to each other and the both gases are heated by the intraband absorption in the corresponding energy bands.

In the regime $\hbar\omega \ll 2|\mu_0|$, the tendency is opposite. The temperature $\delta T/T_0$ grows much faster than the relative change of the density Δ which is physically clear since at $\hbar\omega \ll 2|\mu_0|$ the *intraband* transitions dominate. At very large power densities, however, both Δ and $\delta T/T_0$ become quite comparable to each other.

If the case of intrinsic graphene [Fig. 2(b)], the relative density changes are always much larger than the relative change of temperature. The absolute values of Δ are also much larger than in Fig. 2(a). These two features are a simple consequence of the fact that at $\mu_0 = 0$ eV the interband transitions are always dominant and that in equilibrium the density of charge carriers (4) is much smaller than in the doped one. For example, $\Delta \simeq 100$ in Fig. 2(b) corresponds to

approximately the same values of the nonequilibrium electron and holes densities ($n_e = n_h \approx 1.63 \times 10^{13}$ cm^{-2}) as $\Delta \simeq 4$ in Fig. 2(a) ($n_e \approx 1.25 \times 10^{13}$ cm^{-2}, $n_h \approx 1.56 \times 10^{13}$ cm^{-2}).

B. Power dependencies of different physical quantities

Now, we consider how different physical quantities vary with the radiation intensity. We show results for doped ($\mu_0 = -0.2$ eV) and intrinsic graphene ($\mu_0 = 0$ eV).

1. Doped graphene

Figure 3 exhibits the power dependencies of the chemical potentials μ_e and μ_h, temperature T, photoexcited charge carrier density δn, and the absorption coefficient A, in the doped graphene sample with $\mu_0 = -0.2$ eV, under the condition $\hbar\omega > 2|\mu_0|$ when the interband transitions dominate. The ratio of relaxation times is assumed to be $\tau_\epsilon/\tau_{\rm rec} = 0.1$ and we consider a relatively high-mobility sample with $E_i = 30$ meV (this corresponds to $N_i \approx 6.4 \times 10^{11}$ cm^{-2} and $\mu \approx 7260$ cm^2/Vs, see Fig. 12). At low intensities $I/I_0 \lesssim 10^4$ (left panels), the density δn substantially changes, as expected, while the temperature remains practically unchanged. The chemical potential of electrons quickly grows, from the initial value $\mu_0 = -0.2$ eV, and becomes positive at $I/I_0 \simeq 200$; the chemical potential of holes becomes more negative and varies slowly. The absorption coefficient does not change with the intensity up to $I/I_0 \simeq 10^3$, but starts to decrease when I/I_0 approaches the values of order of 10^4. It is mainly due to the interband contribution, and is about 1%. This number differs from traditional 2.3% since we consider graphene lying on a SiO$_2$ substrate [Eqs. (24) and (25)].

When the intensity grows further, electron and hole gases get heated and the charge carrier temperature increases too. The relative changes of density and temperature become equal at $I/I_0 \approx 5.4 \times 10^6$ [Fig. 3(a), right panel]. At the point where the black and red curves intersect, $\Delta = \delta T/T_0 \approx 2.14$, which corresponds to $n_e \approx 6.68 \times 10^{12}$ cm^{-2}, $n_h \approx 9.80 \times 10^{12}$ cm^{-2}, and $T \approx 3.14 T_0 \approx 942$ K. The chemical potential of electrons continues to grow reaching the values $\simeq +0.26$ eV at $I/I_0 \simeq 10^6$. The chemical potential of holes gets more negative and becomes equal to $\simeq -0.33$ eV at $I/I_0 \simeq 10^6$. Since the occupation of electron and hole states around $\hbar\omega/2 \simeq 0.3$ becomes much less asymmetric as compared to equilibrium, the interband absorption starts to fall down at $I/I_0 \simeq 10^4$ and becomes about 0.04% at $I/I_0 \simeq 10^6$. This strong reduction of the absorption coefficient is usually referred to as the saturable absorption effect. The intraband absorption remains small as compared to the interband one.

Now, we consider the case $\hbar\omega < 2|\mu_0|$ where the intraband absorption plays the crucial role at low intensities. Figure 4 shows the power dependencies of different physical quantities under the same conditions as in Fig. 3 but at $\hbar\omega = 0.1$ eV. Now, the temperature substantially grows at low intensities while the charge carrier density remains almost unchanged up to $I/I_0 \simeq 10^5$ [Fig. 4(a), right panel]. The chemical potential of electrons sharply grows at the radiation power $I/I_0 \lesssim 700$ but then saturates at the much lower level $\mu_e \simeq -0.1$ eV than in Fig. 3. The chemical potential of holes remains almost constant, slightly decreasing in the absolute value. The

absorption coefficient is about 0.12% at low intensities and remains practically constant up to $I/I_0 \simeq 10^5$ [Fig. 4(c)]. It is mainly due to the intraband contribution which is much smaller than in the previous example since the frequency lies in the gap between the intraband and interband absorption areas $\gamma(\mu_0) \ll \omega \ll 2|\mu_0|/\hbar$, where $\hbar\gamma(\mu_0) \approx 4.5$ meV under our conditions. At $I/I_0 \gtrsim 10^5$ the absorption coefficient starts to grow (the induced absorption [48]), mainly due to the interband contribution which becomes essential since the occupation of energy levels at $E \simeq -\hbar\omega/2$ is no longer negligible due to the heating of the hole gas. At $I/I_0 \gtrsim 10^5$ also the chemical potentials of both electrons and holes start to substantially grow, making the distribution of charge carriers over the bands more uniform; at I/I_0 between $\simeq 10^6$ and 10^8 the chemical potential of electrons even becomes positive [Fig. 4(b), right panel]. At even larger intensities $I/I_0 \gtrsim 10^8$, the chemical potential of holes moves to the conduction band $\mu_h > 0$, while that of electrons becomes negative again [Fig. 4(b), right panel].

In Fig. 5 we further illustrate our results by showing the electron distribution function in the valence and conduction bands at different radiation intensities. Here, one clearly sees a qualitative difference between the charge carrier distributions at $\hbar\omega > 2|\mu_0|$ [Fig. 5(a)] and at $\hbar\omega < 2|\mu_0|$ [Fig. 5(b)]. In the interband absorption case $\hbar\omega > 2|\mu_0|$ the slope of the $f(E)$ curves, and hence the charge carrier temperature T, remains practically unchanged up to intensities $I/I_0 \simeq 10^5$. In contrast, the chemical potentials vary quite strongly: already at $I/I_0 \simeq 10^3$ (red curve) the chemical potential of electrons is positive and the occupation of the conduction band is quite large. At higher intensities $I/I_0 \gtrsim 10^6$, when the densities of photoexcited electrons and holes become comparable, the temperature starts to grow too due to the intraband absorption in each band, and the slope of the $f(E)$ curves decreases.

In the intraband absorption case $\hbar\omega < 2|\mu_0|$ [Fig. 5(b)], the slope of the curves noticeably decreases already at $I/I_0 \gtrsim 10^4$, and the occupation of the conduction band is much weaker than in the previous case (the chemical potential of electrons remains negative). Only at the very high intensity $I/I_0 \simeq 10^7$ (magenta curve) μ_e becomes slightly positive.

2. Intrinsic graphene

Figure 6 shows the power dependencies of different physical quantities in intrinsic graphene with $\mu_0 = 0$ and $\hbar\omega = 0.4$ eV. Other parameters (T_0, E_i, and $\tau_\epsilon/\tau_{\rm rec}$) are the same as in Figs. 3, 4, and 5. Since at $\mu_0 = 0$ the condition $\hbar\omega > 2|\mu_0|$ is always satisfied, the curves shown in Fig. 6 are qualitatively similar to those from Fig. 3. The interband transitions dominate, therefore, the relative change of the density Δ is always much larger than the relative change of temperature [Fig. 6(a)]. Only at $I/I_0 \gtrsim 10^6$ the temperature T starts to noticeably grow [Fig. 6(a), right panel]. The chemical potentials of electrons and holes are symmetric, $\mu_e = -\mu_h$, and achieve the values of order $|\mu_e| = |\mu_h| \simeq 0.1$ eV at $I/I_0 \gtrsim 10^4$ and $\simeq 0.2$ eV at $I/I_0 \simeq 10^5 - 10^7$ [Fig. 6(b)]. The absorption curves show the saturable absorption effect: the absorption coefficient A falls down from the value $\simeq 1\%$ at $I/I_0 \lesssim 10^4$ down to the values $\lesssim 0.12\%$ at $I/I_0 \gtrsim 10^6$. The contribution of the intraband absorption to A is negligibly small.
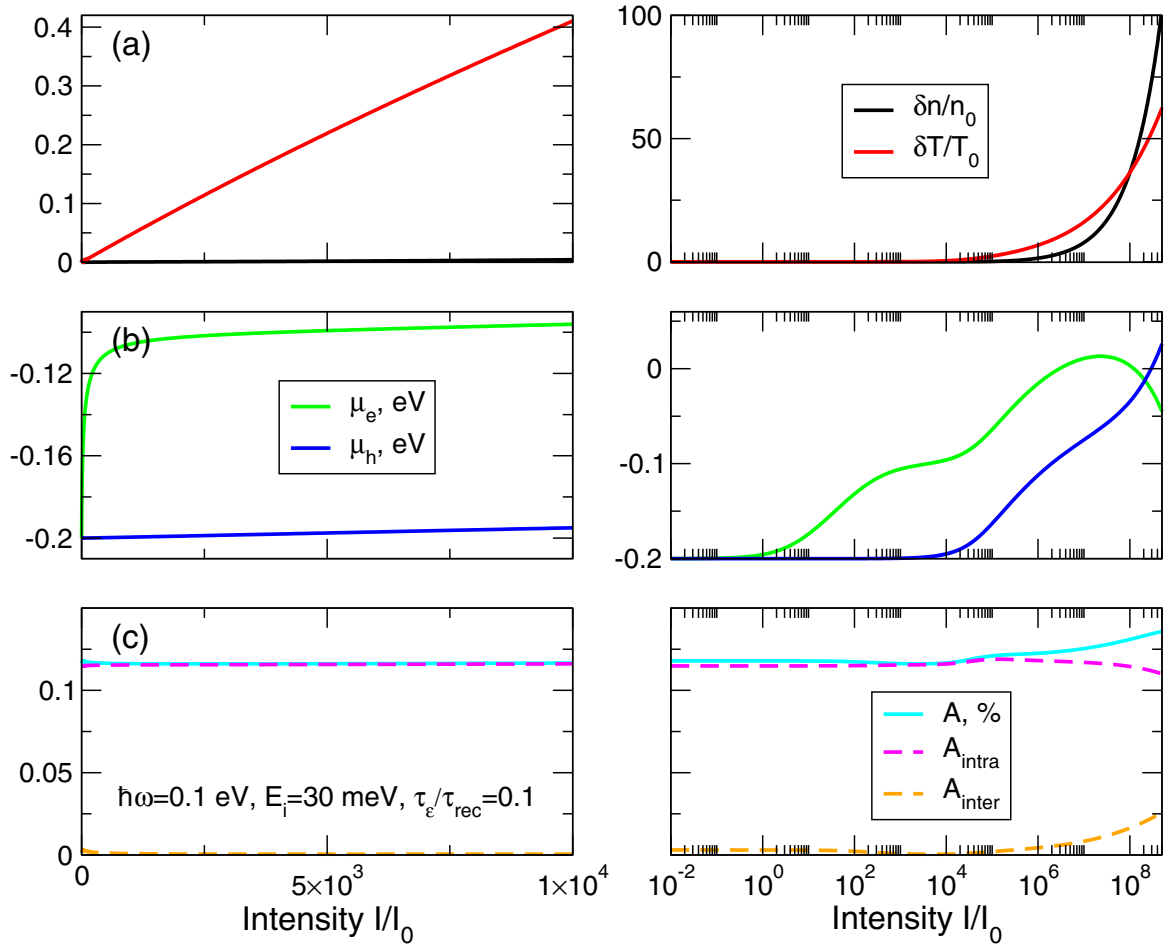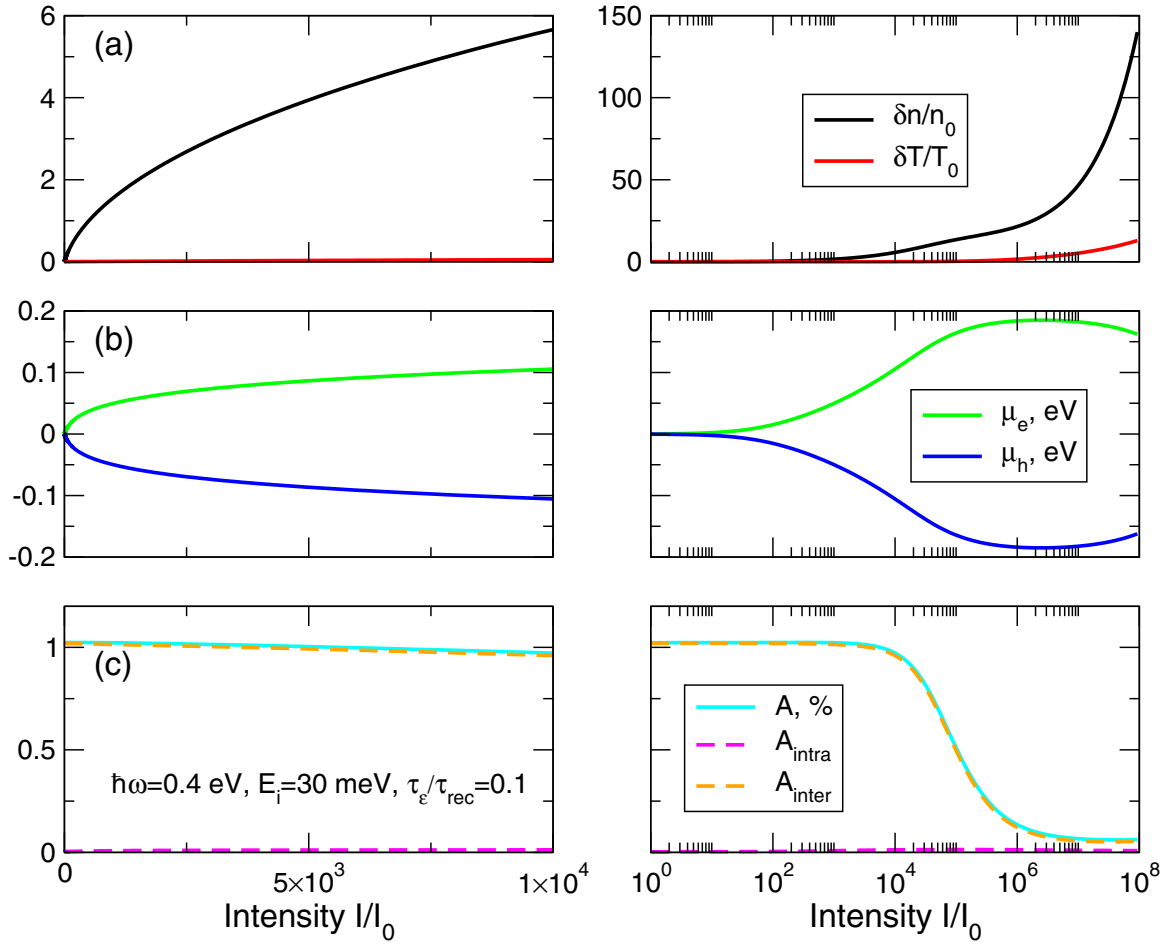
FIG. 4. (a) The relative change of the density $\Delta = \delta n/n_0 = \delta n/(n_e^0 + n_h^0)$ and temperature $(T - T_0)/T_0$, (b) the chemical potentials of electrons and holes μ_e and μ_h, and (c) the absorption coefficient A, together with the intraband and interband contributions, as functions of the dimensionless power density I/I_0 at $\hbar\omega = 0.1$ eV, $E_i = 30$ meV, and $\tau_\epsilon/\tau_{rec} = 0.1$. The equilibrium chemical potential and temperature are $\mu_0 = -0.2$ eV and $T_0 = 300$ K. Left columns show the power dependencies at $I/I_0 < 10^4$, and the right columns the same dependencies in a broader power range. The horizontal axis scale is the same in all left and all right panels. The vertical axis scale is the same in both (c) panels.
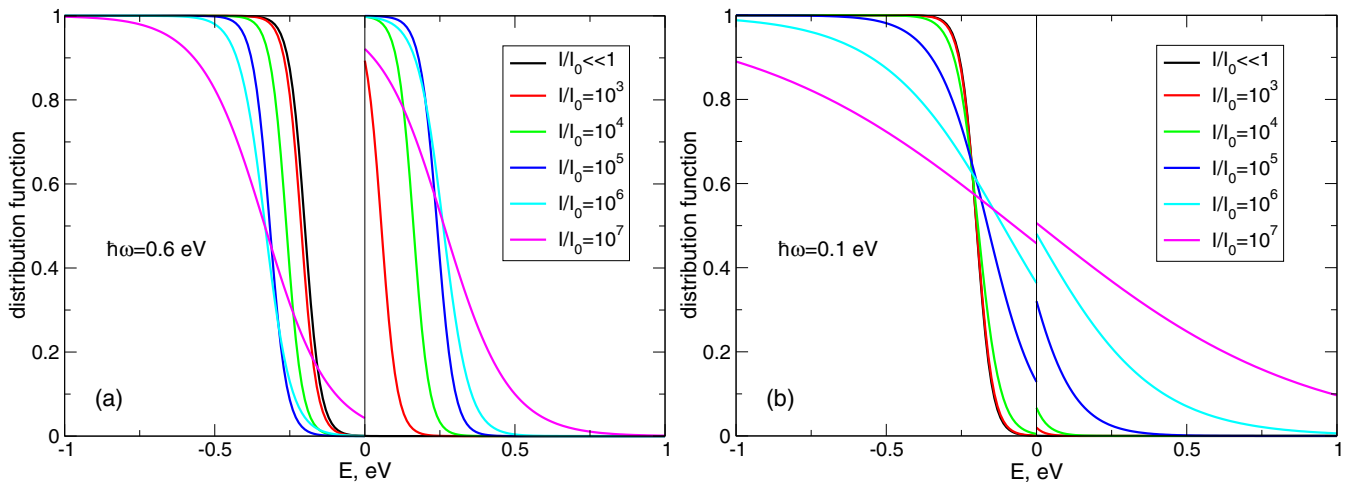
FIG. 5. The electron distribution function (6) in the valence ($E < 0$) and conduction ($E > 0$) bands at different values of the radiation intensity. The radiation frequency is (a) $\hbar\omega = 0.6$ eV and (b) $\hbar\omega = 0.1$ eV, other parameters are $\mu_0 = -0.2$ eV, $T_0 = 300$ K, $E_i = 30$ meV, and $\tau_\epsilon/\tau_{rec} = 0.1$.

FIG. 6. (a) The relative change of the density $\Delta = \delta n/n_0 = \delta n/(n_e^0 + n_h^0)$ and temperature $(T - T_0)/T_0$, (b) the chemical potentials of electrons and holes μ_e and μ_h, and (c) the absorption coefficient A, together with the intraband and interband contributions, as functions of the dimensionless power density I/I_0 at $\hbar\omega = 0.4$ eV, $E_i = 30$ meV, and $\tau_\epsilon/\tau_{\rm rec} = 0.1$. The equilibrium chemical potential and temperature are $\mu_0 = 0$ eV (intrinsic graphene) and $T_0 = 300$ K. Left columns show the power dependencies at $I/I_0 < 10^4$, and the right columns the same dependencies in a broader power range. The horizontal axis scale is the same in all left and all right panels. The vertical axis scale is the same in left and right (b) and (c) panels.
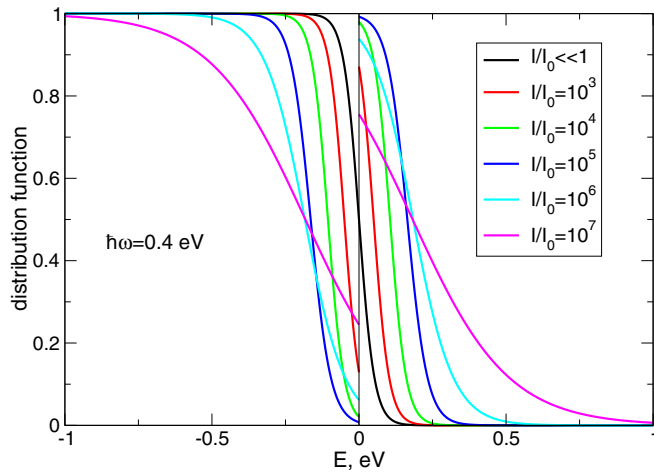

FIG. 7. The electron distribution function (6) in the valence ($E < 0$) and conduction ($E > 0$) bands of intrinsic graphene ($\mu_0 = 0$ eV) at different values of the radiation intensity. Other parameters are $\hbar\omega = 0.4$ eV, $T_0 = 300$ K, $E_i = 30$ meV, and $\tau_\epsilon/\tau_{\rm rec} = 0.1$.

Figure 7 shows the nonequilibrium distribution function of electrons and holes at $\hbar\omega = 0.4$ eV and different power levels. In accordance with Fig. 6 the temperature remains low ($T \simeq T_0$) at the intensities up to $I/I_0 \simeq 10^4$, while the chemical potentials $|\mu_{e,h}|$ grow. At higher intensities, the temperature increases too (the cyan and, especially, magenta curves).

C. Frequency dependencies of different physical quantities

Another way to clarify the physics of the discussed phenomena is to analyze how the frequency dependencies of the absorption coefficient $A(\omega)$ and other physical quantities are modified under the influence of the strong radiation power. This is an especially important question since the spectra $A(\omega)$ can be directly experimentally measured [87].

Figure 8 shows the power-dependent absorption spectra in (a) doped ($|\mu_0| = 0.2$ eV) and (b) intrinsic ($\mu_0 = 0$ eV) graphene, at $\tau_\epsilon/\tau_{\rm rec} = 0.1$, $E_i = 30$ meV, and $T_0 = 300$ K. The black curves in both panels exhibit the known linear response absorption curves (e.g., Refs. [30,87]) corresponding to the equilibrium chemical potential $\mu_e = \mu_h = \mu_0$ and
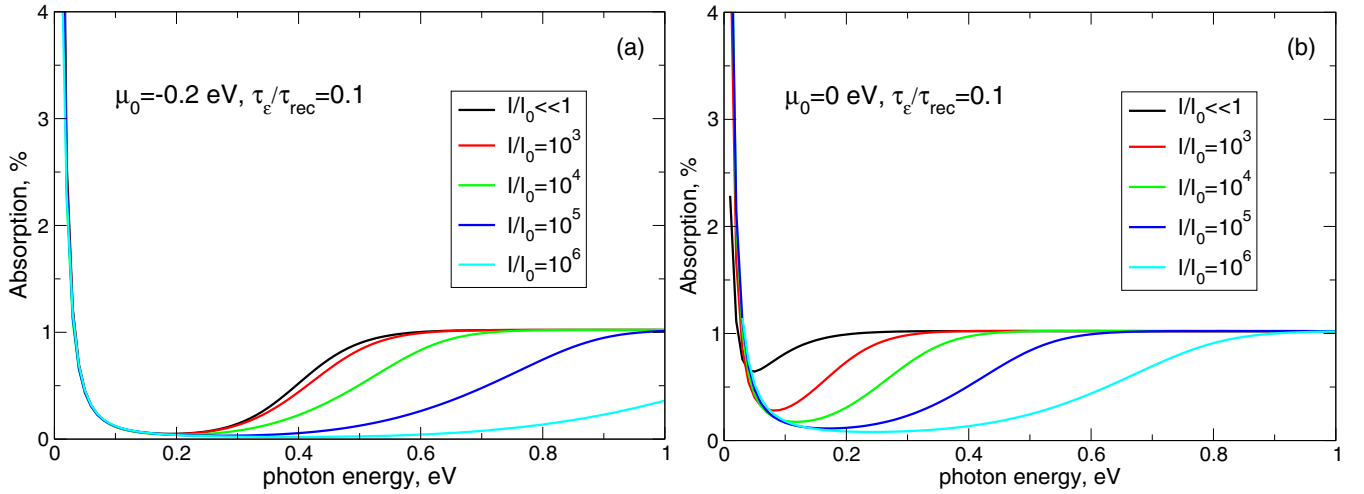
FIG. 8. The absorption coefficient vs frequency at different values of the radiation intensity, for (a) $|\mu_0| = 0.2$ eV and (b) $\mu_0 = 0$ eV. Other parameters are $\tau_\epsilon/\tau_{rec} = 0.1$, $E_i = 30$ meV, and $T_0 = 300$ K.

equilibrium temperature $T = T_0$. One sees that the growing power substantially reduces the absorption in graphene. This *saturable absorption* effect is the case already at $\hbar\omega \gtrsim |\mu_0|$ (not $2|\mu_0|$!) in Fig. 8(a) and at $\hbar\omega \gtrsim 0.04$ eV in Fig. 8(b). The influence of the radiation power is noticeable at $I/I_0 \simeq 10^3$ in the doped graphene [Fig. 8(a)] and at even lower powers ($I/I_0 \simeq 10^1$–10^2) in the intrinsic graphene [Fig. 8(b)]. Quantitatively, the suppression of $A(\omega)$ is very strong; for example, in doped graphene at $\hbar\omega = 0.6$ eV and $I/I_0 = 10^6$ the absorption is only 0.042%, i.e., it is reduced by a factor of ~24. In the intrinsic graphene at $\hbar\omega = 0.3$ eV and $I/I_0 = 10^6$ the absorption is reduced down to 0.085%, i.e., by a factor of ~12. The saturable absorption effect at high frequencies ($\hbar\omega \gtrsim |\mu_0|$) was experimentally observed in many experiments (see, e.g., Refs. [46–50]).

At lower frequencies ($\hbar\omega \lesssim |\mu_0|$) our model predicts an essentially different behavior. The absorption spectrum weakly depends on the radiation power at $\hbar\omega \lesssim |\mu_0|$ and the radiation may lead to a *slight increase* of the absorption. In doped graphene, Figure 8(a), this effect is rather small; for example, at $\hbar\omega = 0.1$ eV the absorption coefficient is about 11.79% at $I/I_0 \ll 1$ and increases by $\simeq 0.3\%$ at $I/I_0 = 10^5$ and by $\simeq 0.45\%$ at $I/I_0 = 10^6$. In intrinsic graphene, Figure 8(b), the growth of absorption is stronger and can achieve 2–3% at I/I_0 up to $\simeq 10^4$: for example, at $\hbar\omega = 0.01$ eV the absorption is about 2.3% at $I/I_0 \ll 1$, 4.8% at $I/I_0 = 10^3$ and 5.8% at $I/I_0 = 10^4$. The specific numbers of the absorption change depend of course on the chosen parameters of the structure.

Physically, the growth of absorption at $\hbar\omega \lesssim 2|\mu_0|$ and its reduction at $\hbar\omega \gtrsim 2|\mu_0|$ are explained by the radiation-induced redistribution of electrons over quantum states in the conduction and valence bands (Fig. 9). Notice that this qualitative picture, which appeared in many publications (see, e.g.,
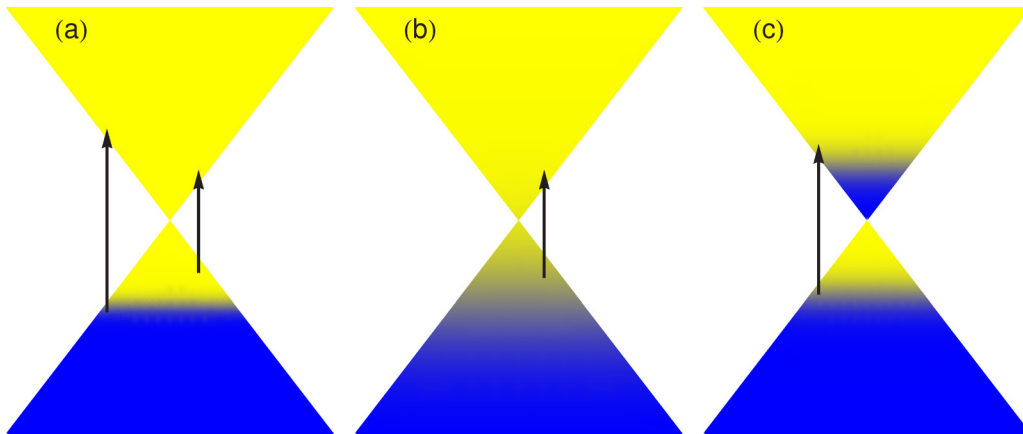

FIG. 9. Interband transitions in graphene (a) in equilibrium and under (b) low-frequency and (c) high-frequency powerful irradiation at a negative chemical potential $\mu_0 < 0$ and low temperature T_0. (a) In equilibrium, the high-frequency photons are absorbed (left arrow: electrons jump from occupied initial to the empty final states) and the low-frequency photons are not (right arrow: initial states are empty). (b) Under the low-frequency powerful irradiation, the electron gas gets heated due to the intraband absorption $T_0 \to T$, the initial states in the valence band get partly occupied, and the interband absorption increases (induced absorption). (c) Under the high-frequency powerful irradiation, the final states in the conduction band get partly occupied and the interband absorption decreases (absorption saturation).
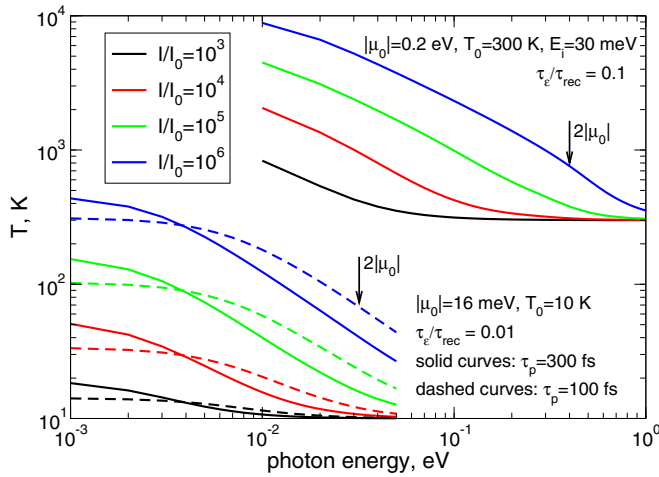
FIG. 10. The hot electron temperature T as a function of the photon energy. Four curves in the upper right corner are plotted for parameters corresponding to Fig. 8(a). The curves in the lower left corner are plotted for parameters of the experiment [48] (see discussion in the text). Arrows indicate the positions of the double chemical potential $2|\mu_0|$.

Ref. [48]), implies that the hot electron temperature T, as well as the chemical potentials of electrons and holes μ_e and μ_h, essentially depend on the photon energy. Within our HEM we can quantitatively evaluate these dependencies. In Fig. 10 we plot the hot electron temperature T as a function of the photon energy for a few sets of experimental parameters. The four curves in the upper right corner show the dependencies $T(\omega)$ for parameters corresponding to Fig. 8(a) ($|\mu_0| = 0.2$ eV, $T_0 = 300$ K, $E_i = 30$ meV, and $\tau_\epsilon/\tau_{rec} = 0.1$) and four different power levels. The arrow labeled as $2|\mu_0|$ indicates the position of the double chemical potential. One sees that at $\hbar\omega \gtrsim 2|\mu_0|$, all curves tend to the equilibrium temperature value $T \to T_0 = 300$ K. Even if at low frequencies the hot electron temperature exceeds T_0 by more than one order of magnitude, at $\hbar\omega \simeq 2|\mu_0|$ it is already almost equal to T_0; for example, for $I/I_0 = 10^5$ (green curve) the temperature T

drops from 4486 K at $\hbar\omega = 10$ meV down to 380 K at $\hbar\omega = 2|\mu_0| = 0.4$ eV.

In a recent experiment on multilayer epitaxial graphene [48], the influence of a strong (pump) radiation on the transmission coefficient of the weak (probe) wave was studied, and a few-percent increase (decrease) of absorption was observed at $\hbar\omega \lesssim 2|\mu_0|$ ($\hbar\omega \gtrsim 2|\mu_0|$). Graphene was weakly doped (μ_0 was evaluated to be $\simeq 13$ meV) and the experiment was performed at 10 K. The pump radiation with the fluence up to $\simeq 1$ μJ/cm^2 reduced the absorption coefficient by a few percent at $\hbar\omega = 30$ meV and increased it by a few percent at $\hbar\omega = 20$ meV. The authors interpreted their results applying a *simplified* HEM which assumed that the chemical potentials remain unchanged under the action of radiation, $\mu_e = \mu_h = \mu_0$, and the hot electron temperature does not depend on the radiation frequency $T(\omega) = $ const. A similar effect was observed and the same interpretation was applied to its explanation in Ref. [45], where the nonlinear absorption in graphene was measured under different equilibrium conditions with $\mu_0 = -0.4$ eV and $T_0 = 300$ K.

As we have seen above, in reality the quantities T, μ_e, and μ_h cannot be considered as frequency independent and a more general theory should be applied. In Fig. 11(a) we plot the absorption spectra calculated for $|\mu_0| = 16$ meV, $T_0 = 10$ K, $\tau_p = 300$ fs, and $\tau_\epsilon/\tau_{rec} = 0.01$; the results were found to be weakly dependent on τ_ϵ/τ_{rec} as long as this parameter is small as compared to unity. To calculate the graphene conductivity and the absorption coefficient, we used the model of the energy-independent momentum scattering time (20) with τ_p taken from Ref. [48]. One sees that the curves corresponding to different power levels intersect at one point lying approximately at $\hbar\omega \approx 28$ meV. This value is smaller than $2|\mu_0| = 32$ meV (in contrast to the results of the simplified HEM, see Ref. [48]); this difference results from strong frequency dependence of $T(\omega)$, shown in the lower left corner of Fig. 10. Right and left from 28 meV the absorption decreases and increases, respectively, and we have chosen the chemical potential $|\mu_0| = 16$ meV to get approximately equal (in absolute values) changes of the absorption coefficient at $\hbar\omega = 20$ and 30 meV. This quantity is slightly larger than
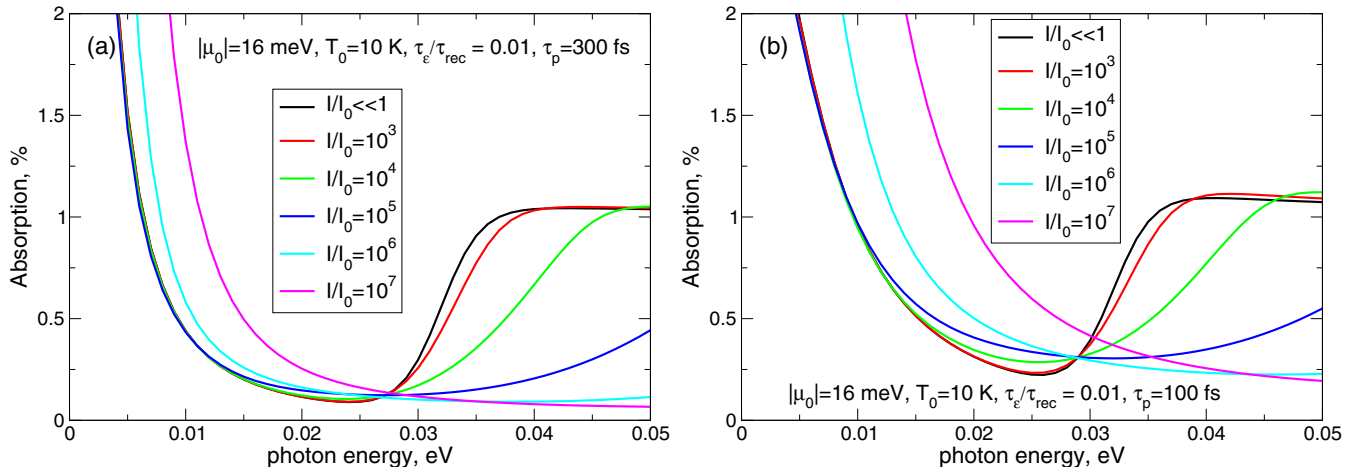

FIG. 11. (a) The absorption coefficient A as a function of the radiation frequency at $\tau_\epsilon/\tau_{rec} = 0.01$, $|\mu_0| = 16$ meV, $T_0 = 10$ K, and (a) $\tau_p = 300$ fs and (b) $\tau_p = 100$ fs.

$|\mu_0| = 13$ meV extracted in Ref. [48] from the comparison of experimental data with the simplified HEM; the reason is again due to the frequency-dependent (-independent) hot electron temperature in the full (simplified) HEM. In general, one sees that our HEM gives reasonable results which can be used for analysis of different nonlinear optics experiments.

As seen from Fig. 11(a) the reduction of absorption right from the intersection point (28 meV) is in general stronger than its growth left from this point. Qualitatively, this is also in agreement with the experimental results of Ref. [48] [see Figs 3(a) and 3(b) there]. Physically, the increase of absorption at low frequencies is due to the larger intraband contribution to A. This contribution can be increased in samples with a lower mobility: in graphene layers with smaller values of τ_p, i.e., with a lower mobility, the hot electron temperature and the absorption increase at low frequencies should be larger. This is confirmed indeed in Fig. 11(b) which shows the absorption spectra for the same parameters as in Fig. 11(a) but for three times smaller $\tau_p = 100$ fs. One sees that the absorption change increases by several times at $\hbar\omega = 20$ meV while at $\hbar\omega \gtrsim 30$ meV changes are less dramatic. Figure 10 also confirms that at frequencies around $2|\mu_0|$ the temperature T is larger in samples with $\tau_p = 100$ fs than in those with $\tau_p = 300$ fs.

IV. SUMMARY

Experiments on the nonlinear graphene optics are very often performed at so strong excitation powers that the perturbation theory fails to adequately describe their results. The hot electron model presented in this paper allows to calculate the most important parameters of highly nonequilibrium charge carriers in graphene, the chemical potentials of electrons and holes, as well as their effective temperature, thus enabling to correctly describe its response to the powerful electromagnetic radiation. The model is physically transparent and employs essentially one fitting parameter: the ratio τ_ϵ/τ_{rec} of the intraband energy relaxation time τ_ϵ to the interband recombination time τ_{rec}. The derived system of strongly nonlinear differential equations (29) and (35)–(39) allows to calculate all physical quantities characterizing the nonlinear graphene response as functions of the incident wave frequency and power, equilibrium temperature, doping level, sample mobility, dielectric environment, and so on. The developed theory reasonably describes available experimental data. Together with the already published perturbative theories of the nonlinear graphene response [28–30], the work done here paves the way to a more accurate interpretation of nonlinear optics experiments and to the development of new optoelectronic devices for visible, infrared, and terahertz spectral ranges.

APPENDIX: A MODEL FOR THE INTRABAND SCATTERING RATE

In order to calculate the intraband conductivity, we need a model for the energy-dependent intraband momentum relaxation rate $\gamma_{intra}(E)$. It is known [88] that the most important scattering mechanism of electrons in graphene is the charged impurity scattering, and that at high energies $\gamma_{intra}(E)$ is proportional to $N_i/|E|$, where N_i is the impurity density. This can be written in the form [89,90]

$$\hbar\gamma_{intra}(E) = \frac{E_i^2}{|E|}, \quad |E| \gtrsim E_i, \quad (A1)$$

where

$$E_i = \alpha\frac{e^2}{\kappa}\sqrt{\pi N_i} \quad (A2)$$

is the Coulomb energy associated with the impurity density N_i, κ is the effective dielectric constant of the medium surrounding the graphene layer, and α is a number of order unity. In Ref. [90] the formula $\alpha = 2\sqrt{I_0(r_s)}$ was derived, where

$$r_s = \frac{e^2}{\kappa\hbar v_F} \quad (A3)$$

is the effective fine-structure constant of graphene and

$$I_0(r_s) = \int_0^1 dx\frac{x^2\sqrt{1-x^2}}{(x+2r_s)^2}. \quad (A4)$$

If graphene lies on the surface of silicon dioxide $\kappa_{SiO_2} = 3.9$, the effective dielectric constant is $\kappa = (\kappa_{SiO_2} + 1)/2 = 2.45$ and $r_s \approx 0.896$. Then, $\alpha \approx 0.36$.

The formula (A1) is not valid at small energies (below E_i). We assume that it can be generalized as follows:

$$\hbar\gamma_{intra}(E) = \frac{\hbar}{\tau_{intra}(E)} = \frac{|E|}{\frac{\zeta}{2} + \sqrt{1 + \frac{E^4}{E_i^4} - 1}}, \quad (A5)$$

where ζ is a number of order unity. Substituting the model expression (A5) into the equilibrium ($\mu_e = \mu_h = \mu_0$) static
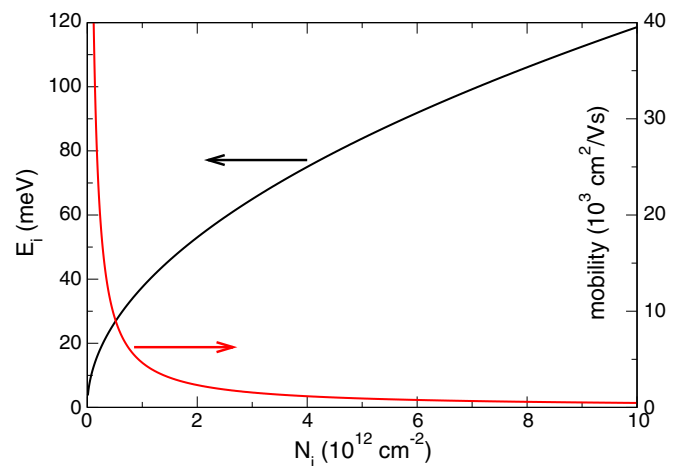

FIG. 12. The Coulomb impurity energy E_i (in meV) and the mobility μ as a function of the impurity density N_i. Graphene is assumed to lie on a SiO$_2$ substrate so that $\kappa = 2.45$, $\alpha = 0.36$, and $\beta = 9.61$.
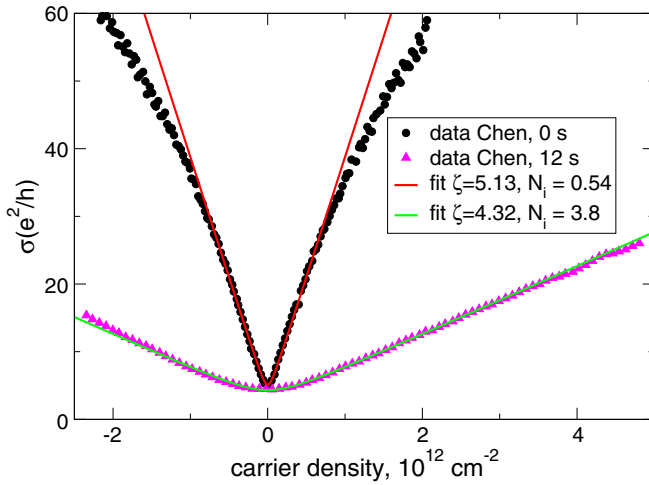
FIG. 13. Experimental data from Ref. [91] for two different potassium atom densities, corresponding to 0-s and 12-s doping times (see Fig. 2 in Ref. [91]). Symbols correspond to the experimental data, solid curves correspond to Eq. (A6) for parameters ζ and N_i indicated on the plot. The density of charge carriers n_s and of impurities N_i are in units 10^{12} cm^{-2}, the conductivity is in units e^2/h.

($\hbar\omega = 0$) zero-temperature ($T = 0$, $\mu_0 = E_F$) intraband conductivity (16) or (17) we obtain

$$\frac{\sigma_{\text{intra}}^{(1)}(0, E_F, 0)}{(e^2/h)} = \zeta + 2\left(\sqrt{1 + \frac{E_F^4}{E_i^4}} - 1\right)$$

$$= \zeta + 2\left(\sqrt{1 + \left(\beta\frac{n_s}{N_i}\right)^2} - 1\right), \quad (A6)$$

where $n_s = k_F^2/\pi = E_F^2/\pi(\hbar v_F)^2$ is the charge carrier density at $T = 0$ and

$$\beta = (\alpha r_s)^{-2} \approx 9.61 \quad (A7)$$

is another numerical factor. As seen from (A6), the factor ζ determines the minimal conductivity of graphene at the Dirac point; in typical experiments $\zeta \simeq 4$. At large densities,

$\beta n_s \gg N_i$, the conductivity in (A6) is proportional to n_s, $\sigma_{\text{intra}}^{(1)}(0, E_F, 0) = e\mu n_s$, which gives the relation between the low-temperature mobility μ and the density of impurities,

$$\mu = \frac{\beta}{\pi}\frac{e}{\hbar N_i}. \quad (A8)$$

Figure 12 illustrates the relations (A2) and (A8) between the impurity density N_i, the energy E_i, and the mobility μ.

Varying two adjustable parameters ζ and E_i one can now fit the expression (A6) to experimental data on the density (or gate-voltage) dependence of the intraband *static* conductivity and then use thus found parameters ζ and E_i for calculations of the *high-frequency* linear and nonlinear responses. In Fig. 13 we illustrate this procedure by fitting (A6) to some of the experimental data from Ref. [91]. In that paper the authors measured the graphene conductivity as a function of gate voltage in samples intentionally doped by potassium atoms. The black and magenta symbols in Fig. 13 show the data from Fig. 2 of Ref. [91], for pristine graphene (denoted as 0 s) and for the same sample after the doping during 12 s. The data from Ref. [91] are replotted as a function of charge carrier density

$$n_s = c_g(V_g - V_{g0})/e, \quad (A9)$$

where the gate capacitance per unit area $c_g = 1.15 \times 10^{-4}$ F/m^2 is taken from Ref. [91]. One sees that the curves (A6) excellently reproduce experimental data at reasonable values of the fitting parameters ζ and N_i. The found values of N_i are about $N_i \approx 0.54 \times 10^{12}$ cm^{-2} for pristine graphene (black symbols) and $N_i \approx 3.8 \times 10^{12}$ cm^{-2} for the doping time of 12 s (magenta symbols). The maximum impurity density (for 18-s doping time) was estimated in Ref. [91] as $(1.4–1.8) \times 10^{-3}$ potassium per carbon, or $N_i^{\text{max}} \simeq (5.3–6.9) \times 10^{12}$ cm^{-2}, which agrees very well with the numbers obtained from our fit.

In the main text we use the energy E_i as a fitting parameter, instead of N_i. If N_i varies in the range $\sim(0.5–5) \times 10^{12}$ cm^{-2}, the energy E_i lies in the interval from $\sim$26.5 to $\sim$83.9 meV and the mobility in the interval from 9300 to 930 cm^2/Vs.

[1] S. A. Mikhailov, Non-linear electromagnetic response of graphene, Europhys. Lett. **79**, 27002 (2007).

[2] S. A. Mikhailov and K. Ziegler, Non-linear electromagnetic response of graphene: Frequency multiplication and the self-consistent field effects, J. Phys.: Condens. Matter **20**, 384204 (2008).

[3] J. J. Dean and H. M. van Driel, Second harmonic generation from graphene and graphitic film, Appl. Phys. Lett. **95**, 261910 (2009).

[4] J. J. Dean and H. M. van Driel, Graphene and few-layer graphite probed by second-harmonic generation: Theory and experiment, Phys. Rev. B **82**, 125411 (2010).

[5] D. A. Smirnova, I. V. Shadrivov, A. E. Miroshnichenko, A. I. Smirnov, and Y. S. Kivshar, Second-harmonic generation by a graphene nanoparticle, Phys. Rev. B **90**, 035412 (2014).

[6] N. A. Savostianova and S. A. Mikhailov, Giant enhancement of the third harmonic in graphene integrated in a layered structure, Appl. Phys. Lett. **107**, 181104 (2015).

[7] Y. Wang, M. Tokman, and A. Belyanin, Second-order nonlinear optical response of graphene, Phys. Rev. B **94**, 195442 (2016).

[8] H. Rostami and M. Polini, Theory of third-harmonic generation in graphene: A diagrammatic approach, Phys. Rev. B **93**, 161411(R) (2016).

[9] J. L. Cheng, N. Vermeulen, and J. E. Sipe, Second order optical nonlinearity of graphene due to electric quadrupole and magnetic dipole effects, Sci. Rep. **7**, 43843 (2017).

[10] N. A. Savostianova and S. A. Mikhailov, Third harmonic generation from graphene lying on different substrates: optical-phonon resonances and interference effects, Opt. Express **25**, 3268 (2017).

[11] S. A. Mikhailov, Theory of the nonlinear optical frequency mixing effect in graphene, Phys. E (Amsterdam) **44**, 924 (2012).

[12] X. Yao, M. Tokman, and A. Belyanin, Efficient Nonlinear Generation of THz Plasmons in Graphene and Topological Insulators, Phys. Rev. Lett. **112**, 055501 (2014).

[13] M. Tokman, Y. Wang, I. Oladyshkin, A. R. Kutayiah, and A. Belyanin, Laser-driven parametric instability and generation of entangled photon-plasmon states in graphene, Phys. Rev. B **93**, 235422 (2016).

[14] J. L. Cheng, N. Vermeulen, and J. E. Sipe, Dc current induced second order optical nonlinearity in graphene, Opt. Express **22**, 15868 (2014).

[15] A. Marini, J. D. Cox, and F. J. García de Abajo, Theory of graphene saturable absorption, Phys. Rev. B **95**, 125408 (2017).

[16] N. A. Savostianova and S. A. Mikhailov, Optical Kerr effect in graphene: Theoretical analysis of the optical heterodyne detection technique, Phys. Rev. B **97**, 165424 (2018).

[17] S. A. Mikhailov, Nonlinear cyclotron resonance of a massless quasiparticle in graphene, Phys. Rev. B **79**, 241309(R) (2009).

[18] X. H. Yao and A. Belyanin, Nonlinear optics of graphene in a strong magnetic field, J. Phys.: Condens. Matter **25**, 054203 (2013).

[19] M. D. Tokman, M. A. Erukhimova, and A. Belyanin, Nonlinear cyclotron acceleration of massless Dirac charge carriers in graphene and topological insulators, JETP Lett. **100**, 390 (2014).

[20] S. A. Mikhailov, Theory of the giant plasmon-enhanced second-harmonic generation in graphene and semiconductor two-dimensional electron systems, Phys. Rev. B **84**, 045432 (2011).

[21] S. A. Mikhailov and D. Beba, Nonlinear broadening of the plasmon linewidth in a graphene stripe, New J. Phys. **14**, 115024 (2012).

[22] N. M. R. Peres, Y. V. Bludov, J. E. Santos, A.-P. Jauho, and M. I. Vasilevskiy, Optical bistability of graphene in the terahertz range, Phys. Rev. B **90**, 125425 (2014).

[23] J. D. Cox and F. J. G. de Abajo, Electrically tunable nonlinear plasmonics in graphene nanoislands, Nat. Commun. **5**, 5725 (2014).

[24] J. D. Cox and F. J. G. de Abajo, Plasmon-enhanced nonlinear wave mixing in nanostructured graphene, ACS Photonics **2**, 306 (2015).

[25] J. D. Cox, I. Silviero, and F. J. G. de Abajo, Quantum effects in the nonlinear response of graphene plasmons, ACS Nano **10**, 1995 (2016).

[26] S. A. Mikhailov, Influence of optical nonlinearities on plasma waves in graphene, ACS Photonics **4**, 3018 (2017).

[27] S. A. Mikhailov, Nonperturbative quasiclassical theory of the nonlinear electrodynamic response of graphene, Phys. Rev. B **95**, 085432 (2017).

[28] J. L. Cheng, N. Vermeulen, and J. E. Sipe, Third order optical nonlinearity of graphene, New J. Phys. **16**, 053014 (2014).

[29] J. L. Cheng, N. Vermeulen, and J. E. Sipe, Third-order nonlinearity of graphene: Effects of phenomenological relaxation and finite temperature, Phys. Rev. B **91**, 235320 (2015); **93**, 039904(E) (2016).

[30] S. A. Mikhailov, Quantum theory of the third-order nonlinear electrodynamic effects in graphene, Phys. Rev. B **93**, 085403 (2016).

[31] S. A. Mikhailov, Non-linear graphene optics for terahertz applications, Microelectron. J. **40**, 712 (2009).

[32] K. L. Ishikawa, Nonlinear optical response of graphene in time domain, Phys. Rev. B **82**, 201402(R) (2010).

[33] J. L. Cheng, N. Vermeulen, and J. E. Sipe, Numerical study of the optical nonlinearity of doped and gapped graphene: From weak to strong field excitation, Phys. Rev. B **92**, 235307 (2015).

[34] B. Semnani, A. H. Majedi, and S. Safavi-Naeini, Nonlinear quantum optical properties of graphene: the role of chirality and symmetry, J. Opt. **18**, 035402 (2016).

[35] S. A. Mikhailov, Equations of macroscopic electrodynamics for two-dimensional crystals, APL Photonics **4**, 034501 (2019).

[36] M. Dragoman, D. Neculoiu, G. Deligeorgis, G. Konstantinidis, D. Dragoman, A. Cismaru, A. A. Muller, and R. Plana, Millimeter-wave generation via frequency multiplication in graphene, Appl. Phys. Lett. **97**, 093101 (2010).

[37] A. Y. Bykov, T. V. Murzina, M. G. Rybin, and E. D. Obraztsova, Second harmonic generation in multilayer graphene induced by direct electric current, Phys. Rev. B **85**, 121413(R) (2012).

[38] N. Kumar, J. Kumar, C. Gerstenkorn, R. Wang, H.-Y. Chiu, A. L. Smirl, and H. Zhao, Third harmonic generation in graphene and few-layer graphite films, Phys. Rev. B **87**, 121406(R) (2013).

[39] S.-Y. Hong, J. I. Dadap, N. Petrone, P.-C. Yeh, J. Hone, and R. M. Osgood, Jr., Optical Third-Harmonic Generation in Graphene, Phys. Rev. X **3**, 021014 (2013).

[40] G. Soavi, G. Wang, H. Rostami, D. G. Purdie, D. De Fazio, T. Ma, B. Luo, J. Wang, A. K. Ott, D. Yoon, S. A. Bourelle, J. E. Muench, I. Goykhman, S. Dal Conte, M. Celebrano, A. Tomadin, M. Polini, G. Cerullo, and A. C. Ferrari, Broadband, electrically tuneable third-harmonic generation in graphene, Nat. Nanotechnol. **13**, 583 (2018).

[41] E. Hendry, P. J. Hale, J. J. Moger, A. K. Savchenko, and S. A. Mikhailov, Coherent Nonlinear Optical Response of Graphene, Phys. Rev. Lett. **105**, 097401 (2010).

[42] T. Gu, N. Petrone, J. F. McMillan, A. van der Zande, M. Yu, G. Q. Lo, D. L. Kwong, J. Hone, and C. W. Wong, Regenerative oscillation and four-wave mixing in graphene optoelectronics, Nat. Photonics **6**, 554 (2012).

[43] K. Alexander, N. A. Savostianova, S. A. Mikhailov, B. Kuyken, and D. Van Thourhout, Electrically tunable optical nonlinearities in graphene-covered SiN waveguides characterized by four-wave mixing, ACS Photonics **4**, 3039 (2017).

[44] J. C. König-Otto, Y. Wang, A. Belyanin, C. Berger, W. A. de Heer, M. Orlita, A. Pashkin, H. Schneider, M. Helm, and S. Winnerl, Four-wave mixing in Landau-quantized graphene, Nano Lett. **17**, 2184 (2017).

[45] K. Alexander, N. A. Savostianova, S. A. Mikhailov, D. Van Thourhout, and B. Kuyken, Gate-tunable nonlinear refraction and absorption in graphene- covered silicon nitride waveguides, ACS Photonics **5**, 4944 (2018).

[46] Q. Bao, H. Zhang, Y. Wang, Z. Ni, Y. Yan, Z. X. Shen, K. P. Loh, and D. Y. Tang, Atomic-layer graphene as a saturable absorber for ultrafast pulsed lasers, Adv. Funct. Mater. **19**, 3077 (2009).

[47] H. Zhang, D. Y. Tang, L. M. Zhao, Q. L. Bao, and K. P. Loh, Large energy mode locking of an erbium-doped fiber laser with atomic layer graphene, Opt. Express **17**, 17630 (2009).

[48] S. Winnerl, M. Orlita, P. Plochocka, P. Kossacki, M. Potemski, T. Winzer, E. Malic, A. Knorr, M. Sprinkle, C. Berger, W. A. de Heer, H. Schneider, and M. Helm, Carrier Relaxation in Epitaxial Graphene Photoexcited Near the Dirac Point, Phys. Rev. Lett. **107**, 237401 (2011).

[49] Z. Zheng, C. Zhao, S. Lu, Y. Chen, Y. Li, H. Zhang, and S. Wen, Microwave and optical saturable absorption in graphene, Opt. Express **20**, 23201 (2012).

[50] V. Bianchi, T. Carey, L. Viti, L. Li, E. H. Linfield, A. G. Davies, A. Tredicucci, D. Yoon, P. G. Karagiannidis, L. Lombardi, F. Tomarchio, A. C. Ferrari, F. Torrisi, and M. S. Vitiello, Terahertz saturable absorbers from liquid phase exfoliation of graphite, Nat. Commun. **8**, 15763 (2017).

[51] H. Zhang, S. Virally, Q. L. Bao, L. K. Ping, S. Massar, N. Godbout, and P. Kockaert, Z-scan measurement of the nonlinear refractive index of graphene, Opt. Lett. **37**, 1856 (2012).

[52] W. Chen, W. Guang, S. Qin, C. Wang, J. Fang, J. Qi, X. Zhang, L. Wang, H. Jia, and S. Chang, The nonlinear optical properties of coupling and decoupling graphene layers, AIP Adv. **3**, 042123 (2013).

[53] L. Miao, Y. Jiang, S. Lu, B. Shi, C. Zhao, H. Zhang, and S. Wen, Broadband ultrafast nonlinear optical response of few-layers graphene: toward the mid-infrared regime, Photon Res. **3**, 214 (2015).

[54] E. Dremetsika, B. Dlubak, S.-P. Gorza, C. Ciret, M.-B. Martin, S. Hofmann, P. Seneor, D. Dolfi, S. Massar, P. Emplit, and P. Kockaert, Measuring the nonlinear refractive index of graphene using the optical Kerr effect method, Opt. Lett. **41**, 3281 (2016).

[55] N. Vermeulen, D. Castelló-Lurbe, J. L. Cheng, I. Pasternak, A. Krajewska, T. Ciuk, W. Strupinski, H. Thienpont, and J. Van Erps, Negative Kerr Nonlinearity of Graphene as Seen Via Chirped-Pulse-Pumped Self-Phase Modulation, Phys. Rev. Appl. **6**, 044006 (2016).

[56] A. Tomadin, S. M. Hornett, H. I. Wang, E. M. Alexeev, A. Candini, C. Coletti, D. Turchinovich, M. Kläui, M. Bonn, F. H. L. Koppens, E. Hendry, M. Polini, and K.-J. Tielrooij, The ultrafast dynamics and conductivity of photoexcited graphene at different Fermi energies, Sci. Adv. **4**, eaar5313 (2018).

[57] V. Ryzhii, T. Otsuji, M. Ryzhii, and M. S. Shur, Double graphene-layer plasma resonances terahertz detector, J. Phys. D: Appl. Phys. **45**, 302001 (2012).

[58] X. Gan, R.-J. Shiue, Y. Gao, I. Meric, T. F. Heinz, K. Shepard, J. Hone, S. Assefa, and D. Englund, Chip-integrated ultrafast graphene photodetector with high responsivity, Nat. Photonics **7**, 883 (2013).

[59] X. Wang, Z. Cheng, K. Xu, H. K. Tsang, and J.-B. Xu, High responsivity graphene/silicon-heterostructure waveguide photodetectors, Nat. Photonics **7**, 888 (2013).

[60] A. Pospischil, M. Humer, M. M. Furchi, D. Bachmann, R. Guider, T. Fromherz, and T. Mueller, CMOS-compatible graphene photodetector covering all optical communication bands, Nat. Photonics **7**, 892 (2013).

[61] V. Ryzhii, T. Otsuji, M. Ryzhii, V. Ya. Aleshkin, A. A. Dubinov, D. Svintsov, V. Mitin, and M. S. Shur, Graphene vertical cascade interband terahertz and infrared photodetectors, 2D Mater. **2**, 025002 (2015).

[62] P. Q. Liu, I. J. Luxmoore, S. A. Mikhailov, N. A. Savostianova, F. Valmorra, J. Faist, and G. R. Nash, Highly tunable hybrid metamaterials employing split-ring resonators strongly coupled to graphene surface plasmons, Nat. Commun. **6**, 8969 (2015).

[63] S. J. Kindness, N. W. Almond, B. Wei, R. Wallis, W. Michailow, V. S. Kamboj, P. Braeuninger-Weimer, S. Hofmann, H. E. Beere, D. A. Ritchie, and R. Degl'Innocenti, Active control of electromagnetically induced transparency in a terahertz metamaterial array with graphene for continuous resonance frequency tuning, Adv. Opt. Mater. **6**, 1800570 (2018).

[64] M. Liu, X. Yin, E. Ulin-Avila, B. Geng, T. Zentgraf, L. Ju, F. Wang, and X. Zhang, A graphene-based broadband optical modulator, Nature (London) **474**, 64 (2011).

[65] C. T. Phare, Y.-H. D. Lee, J. Cardenas, and M. Lipson, Graphene electro-optic modulator with 30 GHz bandwidth, Nat. Photonics **9**, 511 (2015).

[66] Z. Sun, T. Hasan, F. Torrisi, D. Popa, G. Privitera, F. Wang, F. Bonaccorso, D. M. Basko, and A. C. Ferrari, Graphene mode-locked ultrafast laser, ACS Nano **4**, 803 (2010).

[67] H. Zhang, D. Tang, R. J. Knize, L. Zhao, Q. Bao, and K. P. Loh, Graphene mode locked, wavelength-tunable, dissipative soliton fiber laser, Appl. Phys. Lett. **96**, 111112 (2010).

[68] D. Popa, Z. Sun, F. Torrisi, T. Hasan, F. Wang, and A. C. Ferrari, Sub 200 fs pulse generation from a graphene mode-locked fiber laser, Appl. Phys. Lett. **97**, 203106 (2010).

[69] D. Popa, Z. Sun, T. Hasan, F. Torrisi, F. Wang, and A. C. Ferrari, Graphene Q-switched, tunable fiber laser, Appl. Phys. Lett. **98**, 073106 (2011).

[70] Q. Bao, H. Zhang, Z. Ni, Y. Wang, L. Polavarapu, Z. Shen, Q.-H. Xu, D. Tang, and K. P. Loh, Monolayer graphene as a saturable absorber in a mode-locked laser, Nano Res. **4**, 297 (2011).

[71] V. Ryzhii, A. Satou, and T. Otsuji, Plasma waves in two-dimensional electron-hole system in gated graphene heterostructures, J. Appl. Phys. **101**, 024509 (2007).

[72] T. Otsuji, S. A. Boubanga Tombet, A. Satou, H. Fukidome, M. Suemitsu, E. Sano, V. Popov, M. Ryzhii, and V. Ryzhii, Graphene-based devices in terahertz science and technology, J. Phys. D: Appl. Phys. **45**, 303001 (2012).

[73] V. Ryzhii, A.A. Dubinov, T. Otsuji, V. Ya. Aleshkin, M. Ryzhii, and M.S. Shur, Double-graphene-layer terahertz laser: concept, characteristics, and comparison, Opt. Express **21**, 31567 (2013).

[74] E. Malic, T. Winzer, E. Bobkin, and A. Knorr, Microscopic theory of absorption and ultrafast many-particle kinetics in graphene, Phys. Rev. B **84**, 205406 (2011).

[75] B. Y. Sun, Y Zhou, and M. W. Wu, Dynamics of photoexcited carriers in graphene, Phys. Rev. B **85**, 125413 (2012).

[76] J. C. W. Song, K. J. Tielrooij, F. H. L. Koppens, and L. S. Levitov, Photoexcited carrier dynamics and impact-excitation cascade in graphene, Phys. Rev. B **87**, 155429 (2013).

[77] A. Tomadin, D. Brida, G. Cerullo, A. C. Ferrari, and M. Polini, Nonequilibrium dynamics of photoexcited electrons in graphene: Collinear scattering, auger processes, and the impact of screening, Phys. Rev. B **88**, 035430 (2013).

[78] C. H. Lui, K. F. Mak, J. Shan, and T. F. Heinz, Ultrafast Photoluminescence from Graphene, Phys. Rev. Lett. **105**, 127404 (2010).

[79] M. Breusing, S. Kuehn, T. Winzer, E. Malić, F. Milde, N. Severin, J. P. Rabe, C. Ropers, A. Knorr, and T. Elsaesser, Ultrafast nonequilibrium carrier dynamics in a single graphene layer, Phys. Rev. B **83**, 153410 (2011).

[80] D. Brida, A. Tomadin, C. Manzoni, Y. J. Kim, A. Lombardo, S. Milana, R. R. Nair, K. S. Novoselov, A. C. Ferrari, G. Cerullo, and M. Polini, Ultrafast collinear scattering and carrier multiplication in graphene, Nat. Commun. **4**, 1987 (2013).

[81] J. C. Johannsen, S. Ulstrup, F. Cilento, A. Crepaldi, M. Zacchigna, C. Cacho, I. C. Edmond Turcu, E. Springate, F. Fromm, C. Raidel, T. Seyller, F. Parmigiani, M. Grioni, and

P. Hofmann, Direct View of Hot Carrier Dynamics in Graphene, Phys. Rev. Lett. **111**, 027403 (2013).

[82] F. T. Vasko and V. Ryzhii, Photoconductivity of intrinsic graphene, Phys. Rev. B **77**, 195433 (2008).

[83] G. Alymov, V. Vyurkov, V. Ryzhii, A. Satou, and D. Svintsov, Auger recombination in dirac materials: A tangle of many-body effects, Phys. Rev. B **97**, 205411 (2018).

[84] J. M. Dawlaty, S. Shivaraman, M. Chandrashekhar, F. Rana, and M. G. Spencer, Measurement of ultrafast carrier dynamics in epitaxial graphene, Appl. Phys. Lett. **92**, 042116 (2008).

[85] P. A. George, J. Strait, J. Dawlaty, S. Shivaraman, M. Chandrashekhar, F. Rana, and M. G. Spencer, Ultrafast optical-pump terahertz-probe spectroscopy of the carrier relaxation and recombination dynamics in epitaxial graphene, Nano Lett. **8**, 4248 (2008).

[86] V. L. Bonch-Bruevich and S. G. Kalashnikov, *The Physics of Semiconductors* (Nauka, Moscow, 1977).

[87] Z. Q. Li, E. A. Henriksen, Z. Jiang, Z. Hao, M. C. Martin, P. Kim, H. L. Stormer, and D. N. Basov, Dirac charge dynamics in graphene by infrared spectroscopy, Nat. Phys. **4**, 532 (2008).

[88] S. Das Sarma, S. Adam, E. H. Hwang, and E. Rossi, Electronic transport in two-dimensional graphene, Rev. Mod. Phys. **83**, 407 (2011).

[89] M. Trushin and J. Schliemann, Minimum Electrical and Thermal Conductivity of Graphene: A Quasiclassical Approach, Phys. Rev. Lett. **99**, 216602 (2007).

[90] E. H. Hwang and S. Das Sarma, Screening-induced temperature-dependent transport in two-dimensional graphene, Phys. Rev. B **79**, 165404 (2009).

[91] J.-H. Chen, C. Jang, S. Adam, M. S. Fuhrer, E. D. Williams, and M. Ishigami, Charged-impurity scattering in graphene, Nat. Phys. **4**, 377 (2008).